

Long-Range Propagation of the Semidiurnal Internal Tide from the Hawaiian Ridge

ZHONGXIANG ZHAO

Applied Physics Laboratory, University of Washington, Seattle, Washington

MATTHEW H. ALFORD

Applied Physics Laboratory, and School of Oceanography, University of Washington, Seattle, Washington

JENNIFER A. MACKINNON AND ROB PINKEL

Scripps Institution of Oceanography, La Jolla, California

(Manuscript received 5 January 2009, in final form 26 October 2009)

ABSTRACT

The northeastward progression of the semidiurnal internal tide from French Frigate Shoals (FFS), Hawaii, is studied with an array of six simultaneous profiling moorings spanning 25.5°–37.1°N (≈ 1400 km) and 13-yr-long Ocean Topography Experiment (TOPEX)/Poseidon (T/P) altimeter data processed by a new technique. The moorings have excellent temporal and vertical resolutions, while the altimeter offers broad spatial coverage of the surface manifestation of the internal tide's coherent portion. Together these two approaches provide a unique view of the internal tide's long-range propagation in a complex ocean environment. The moored observations reveal a rich, time-variable, and multimodal internal tide field, with higher-mode motions contributing significantly to velocity, displacement, and energy. In spite of these contributions, the coherent mode-1 internal tide dominates the northeastward energy flux, and is detectable in both moored and altimetric data over the entire array. Phase and group propagation measured independently from moorings and altimetry agree well with theoretical values. Sea surface height anomalies (SSHAs) measured from moorings and altimetry agree well in amplitude and phase until the northern end of the array, where phase differences arise presumably from refraction by mesoscale flows. Observed variations in SSHA, energy flux, and kinetic-to-potential energy ratio indicate an interference pattern resulting from superposed northeastward radiation from Hawaii and southeastward from the Aleutian Ridge. A simple model of two plane waves explains most of these features.

1. Introduction

Internal tides have been observed for many decades and are the subject of much recent study owing to their potential to mix the deep ocean (e.g., Wunsch 1975; Hendry 1977; St. Laurent and Garrett 2002; Garrett and Kunze 2007). Egbert and Ray (2000, 2001) estimate that about 1 TW of barotropic tidal energy dissipates in the deep ocean over rough topography such as ridges and island chains. The 2500-km-long Hawaiian Ridge is one intensive barotropic-to-baroclinic tide conversion region, over which the energy loss rate of the M_2 barotropic tide is estimated to be 20 ± 6 GW (e.g., Egbert

and Ray 2000, 2001; Rudnick et al. 2003; Lee et al. 2006). Most of this energy is transported away and is associated with low-mode internal tides (e.g., Merrifield and Holloway 2002; Alford 2003; Klymak et al. 2006). Mode-1 internal tides have been observed to propagate thousands of kilometers from their generation sites (e.g., Dushaw et al. 1995; Ray and Cartwright 2001; Alford and Zhao 2007a; Zhao and Alford 2009). Thus, how far the low-mode internal tides propagate (and where and how they dissipate) is a focus of ongoing efforts (e.g., Alford 2003; MacKinnon and Winters 2005; Rainville and Pinkel 2006b; Alford et al. 2007).

In this paper, we examine the long-range propagation of the internal tide northeast of Hawaii as observed using an array of profiling moorings and satellite altimeter measurements. These two techniques are complementary, measuring quite different aspects of the

Corresponding author address: Zhongxiang Zhao, Applied Physics Laboratory, 1013 NE 40th St., Seattle, WA 98105.
E-mail: zzhao@apl.washington.edu

motions. The moorings give a rich depth–time view of the internal tide at a few discrete locations. By contrast, satellite altimeters offer broad spatial coverage, but measure only the surface manifestation of the coherent, mode-1 component, and that at only ≈ 250 km horizontal resolution. Since the moored array was deployed directly beneath a Ocean Topography Experiment (TOPEX)/Poseidon (T/P) track, we conduct a direct comparison. In spite of the differences between the techniques, moored and altimetric sea surface height anomalies (SSHAs) agree remarkably well, facilitating their combined use to construct a synthesized view.

The altimeter observations are of particular value in interpreting our measurements owing to the known difficulty in interpreting point measurements in the presence of multidirectional wave fields (Nash et al. 2006; Martini et al. 2007; Rainville et al. 2010). That is, in contrast to a single propagating wave, which shows constant energy flux, velocity ellipses elongated in the direction of wave propagation, and a constant ratio of horizontal kinetic to available potential energy (HKE/APE), superposed wave trains exhibit interference patterns where all of these quantities change depending on their spatial locations. Our measurements indicate a superposition of northeastward radiation from multiple sources at the Hawaiian Ridge and southeastward radiation from the Aleutian Ridge. A simple two-wave model reproduces many of the observed aspects of the observed interference pattern.

After giving a detailed description of the moored and altimetric data and their processing (section 2), our goals in this paper are threefold: first, to present a qualitative picture of the internal tide in the region (section 3); second, to conduct a detailed comparison of the moored and altimetric techniques (section 4); and finally to demonstrate the manifestation of the Hawaii–Aleutian interference pattern in the moored and altimetric measurements (section 5). A summary (section 6) and a discussion (section 7) follow.

2. Data and methods

From the moored data, we seek to characterize the modal content and the degree of coherence with astronomical forcing of the semidiurnal internal tide versus range from the generation site. To do this, the semidiurnal signals are first isolated via bandpass filtering. The bandpassed velocity and isopycnal displacement signals are then decomposed into the five lowest baroclinic modes. The semidiurnal signals are further decomposed into coherent and incoherent constituents. These methods, mostly quite standard, are described in this section, followed by a description of the T/P altimeter SSHA data and processing methods.

a. The IWAP experiment

The Internal Waves Across the Pacific (IWAP) experiment (Fig. 1; Alford et al. 2007) was designed to follow the northeastward internal tidal beam originating from French Frigate Shoals (FFS), Hawaii, identified in numerical model results from the Primitive Equations Z-coordinate Harmonic Analysis of Tides (PEZHAT) (Fig. 1, yellow arrows, data courtesy of E. Zaron) and Princeton Ocean Model (POM) (data courtesy of S. Johnston, not shown) datasets. IWAP's focus was on the internal tide's long-range propagation, complementing the Hawaii Ocean Mixing Experiment (HOME), which focused on the internal tide's generation and local dissipation at the Hawaiian Ridge. Measurements were conducted spanning moored profiler 1 (MP1) at 25.5°N , about 200 km from the ridge, and MP6 at 37.1°N , over 1600 km away. The experiment consisted of two cruises on board the R/V *Revelle*: the first was from 18 April to 25 May 2006, and the second from 1 to 18 June 2006. Its primary components were 1) an array of six profiling moorings (black dots showing MP1–MP6, described in Tables 1 and 2), 2) a spatial survey (white line), and 3) three high-resolution time series (blue dots). Only the moored data are discussed here.

b. Profiling mooring measurements

The six moorings were identical in their instrument arrangements (see Fig. 2a). From the surface to 40 m, an upward-looking 300-kHz RDI ADCP on the subsurface float measured velocity profiles every 2 min. Between 85 and 1400 m, a McLane MP climbed up and down through the water column along the mooring wire, completing one up or down profile each 1.5 h (left panels of Fig. 3, green line). Each carried a Falmouth Scientific CTD and acoustic current meter, delivering profiles of density and velocity with a vertical resolution of about 2 m (Doherty et al. 1999). At ≈ 3000 m, an Aanderaa RCM8 current meter measured the horizontal velocity every 10 min, and a Sea-Bird temperature logger measured the temperature twice every minute. High wire tension (≈ 500 kg), together with generally weak currents, ensured mooring knockdown was less than 20 m at all sites.

The instruments generally functioned well, with the exception of MP4, where the MP stopped profiling after 23 days because of a broken drive axle, and MP5, where the MP sampled its full range for 4 days and afterward only at 700–1400 m owing to heavy ballasting. In addition, the upward-looking ADCP data at MP5 were lost because of a corrupt flash memory card. Thus, the durations of full-depth time series at MP1, MP2, MP3, and MP6 range between 40 and 50 days, but only 23 and 4 days for MP4 and MP5, respectively (Table 1).

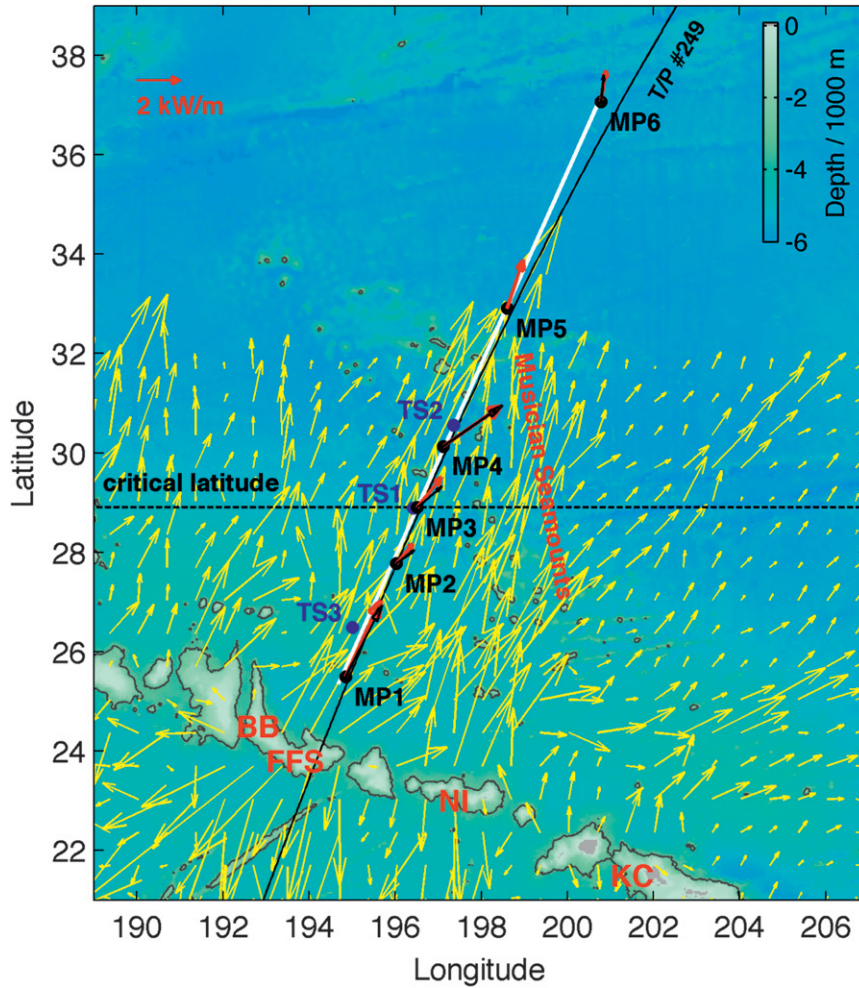


FIG. 1. Bathymetry (colors) of the IWP experiment site. The 3000-m isobath contours are shown in gray, together with the ship track (white line), mooring locations (black dots), and the mooring-measured time-mean mode-1 energy fluxes computed as the bandpassed semidiurnal signals (red arrows) and the coherent portion (black arrows). Four internal tide generation sites are labeled: the Kauai Channel (KC), Nihoa Island (NI), French Frigate Shoals (FFS), and Brooks Banks (BB). Locations of the time series presented in Alford et al. (2007) are shown as blue dots. Yellow arrows are the M_2 energy fluxes from the PEZHAT numerical model (data courtesy of E. Zaron). The dashed line is the critical latitude (28.8°N) for the M_2 internal tide. The black line is T/P track 249.

The measured horizontal velocity is decomposed into along-beam (v) and cross-beam (u) components, with the along-beam direction defined toward 60° north of east, the mean direction of the FFS internal tidal beam. Samples of raw data at MP1, MP3, and MP6 are shown in the left panels of Fig. 3. Colors indicate the along-beam velocities obtained from the ADCP (0–40 m), MP (85–1400 m), and Aanderaa (≈ 3000 m). The Aanderaa-measured velocities are plotted in a 200-m-thick layer on the same color scale. A rich field of low-frequency and near-inertial flows is seen. These flows largely obscure tidal signals, which will be isolated below with harmonic analysis and bandpass filtering.

The sawtooth pattern traced by MP leads to a variable temporal resolution pattern ranging from 3 h at 85 and 1400 m to 1.5 h at middepths (left panels of Fig. 3, green line). The ADCP, Sea-Bird, and Aanderaa data have much higher temporal resolutions, ranging between 0.5 and 10 min. All data are gridded onto uniform 1.5-h temporal and 2-m vertical grids using linear interpolation.

c. Bandpass filtering

The semidiurnal components of the mooring data are extracted by bandpassing data at each depth with a fourth-order Butterworth filter centered at the M_2 tidal frequency ($2.23 \times 10^{-5} \text{ s}^{-1}$) with zero-phase response

TABLE 1. IWAP profiling moorings.

Mooring	Location (°N, °E)	Depth (m)	Time* (day)	Offset from track 249 (km)	Semidiurnal flux**		Coherent flux**		M_2 flux**	
					Magnitude (kW m ⁻¹)	Direction (°)	Magnitude (kW m ⁻¹)	Direction (°)	Magnitude (kW m ⁻¹)	Direction (°)
MP1	25.5, 194.9	4874	41	4	3.48	62.0	3.35	60.6	2.76	62.5
MP2	27.8, 196.0	5461	42	4	1.08	46.8	0.99	36.1	0.71	31.3
MP3	28.9, 196.5	5359	50	10	1.64	47.6	1.44	38.5	1.34	36.5
MP4	30.1, 197.1	5736	23	10	3.26	34.3	3.19	34.0	3.10	29.8
MP5	32.9, 198.6	5968	4	14	2.09	68.7	—	—	—	—
MP6	37.1, 200.8	5810	44	43	1.26	77.7	1.09	81.3	0.97	79.6

*Time gives the number of days a mooring correctly functioned. MP4 stopped profiling early owing to a broken drive shaft. MP5 sampled only the 700–1400-m water column after 4 days owing to heavy ballasting.

** Time-mean depth-integrated fluxes of the mode-1 internal tide for the semidiurnal band, coherent portion, and harmonic M_2 constituent, respectively.

and quarter-power points at $\{2.01, 2.47\} \times 10^{-5} \text{ s}^{-1}$, that is, 1.73–2.13 cpd. This passband includes the M_2 and S_2 tidal constituents but rejects inertial motion, whose frequency ranges between 0.99 and $1.39 \times 10^{-5} \text{ s}^{-1}$ in this latitudinal range.

Semidiurnal signals obtained in this manner are plotted in the right panels of Fig. 3. Note that barotropic currents are also removed as described below (section 2e). Baroclinic semidiurnal currents with amplitudes $O(10 \text{ cm s}^{-1})$ are now seen. Opposing shallow–deep flows at MP1 (Fig. 3b) indicate the dominance of mode-1 motions, with higher-mode contributions becoming more evident to the north (Figs. 3d and 3f). These signals will be considered in detail in section 3.

d. Vertical displacement

From the surface to 1400 m, displacement of a set of isopycnals evenly spaced in depth is computed by linear interpolation of the MP-measured density profiles. Signals associated with long-term density changes are small, but are removed by means of a sliding 5-day window. At $\approx 3000 \text{ m}$, isothermal displacement (assumed equal to the isopycnal displacement) is calculated from the bandpassed Sea-Bird temperature $T(t)$ by $\eta(t) = T(t)/T_z$, where $T_z \approx 2 \times 10^{-4} \text{ °C m}^{-1}$ is the vertical temperature gradient at $\approx 3000 \text{ m}$ from the annual-mean hydrography in the 2005 *World Ocean Atlas* (WOA05; Antonov et al. 2006;

Locarnini et al. 2006). Raw and semidiurnally bandpassed displacements are shown in Fig. 3. Semidiurnal signals (right panels) are more visible in Fig. 3 in the raw displacement than in the raw velocity (left panels), owing to the smaller near-inertial contributions to the displacement.

e. Modal decomposition

The bandpassed semidiurnal signals are next projected onto baroclinic modes. In an ocean of depth H , internal tides can be represented by a superposition of discrete baroclinic modes that depend on the buoyancy frequency profile $N(z)$. The baroclinic modes for vertical displacement, $\Phi(z)$, can be determined by the eigenvalue equation,

$$\frac{d^2\Phi(z)}{dz^2} + \frac{N^2(z)}{c_n^2}\Phi(z) = 0 \quad (1)$$

subject to the boundary conditions $\Phi(0) = \Phi(-H) = 0$, where n is the mode number and c_n is the eigenspeed (Gill 1982).

The corresponding baroclinic modes for pressure and horizontal velocity $\Pi(z)$ are related to $\Phi(z)$ via

$$\Pi(z) = \rho_0 c_n^2 \frac{d\Phi(z)}{dz}, \quad (2)$$

TABLE 2. Propagation time (days) of the mode-1 semidiurnal internal tide from the primary generation source at FFS (24.0°N, 193.5°E) to the six IWAP moorings, at phase and group speeds, respectively.

Mooring	Distance (km)	At M_2 phase			At S_2 phase			At group velocity		
		Mooring	Theory	T/P	Mooring	Theory	T/P	Mooring	Theory	T/P
MP1	218	0.55	0.68	0.58	0.56	0.69	0.59	0.70	0.84	0.77
MP2	490	1.51	1.62	1.47	1.39	1.64	1.49	0.71	2.04	1.95
MP3	621	1.87	2.06	1.89	1.88	2.08	1.92	2.13	2.62	2.52
MP4	766	2.41	2.54	2.36	2.12	2.57	2.38	2.96	3.27	3.14
MP5	1108	3.43	3.67	3.44	3.46	3.71	3.48	4.17	4.85	4.60
MP6	1614	4.96	5.34	5.06	4.99	5.40	5.12	7.33	7.43	6.81

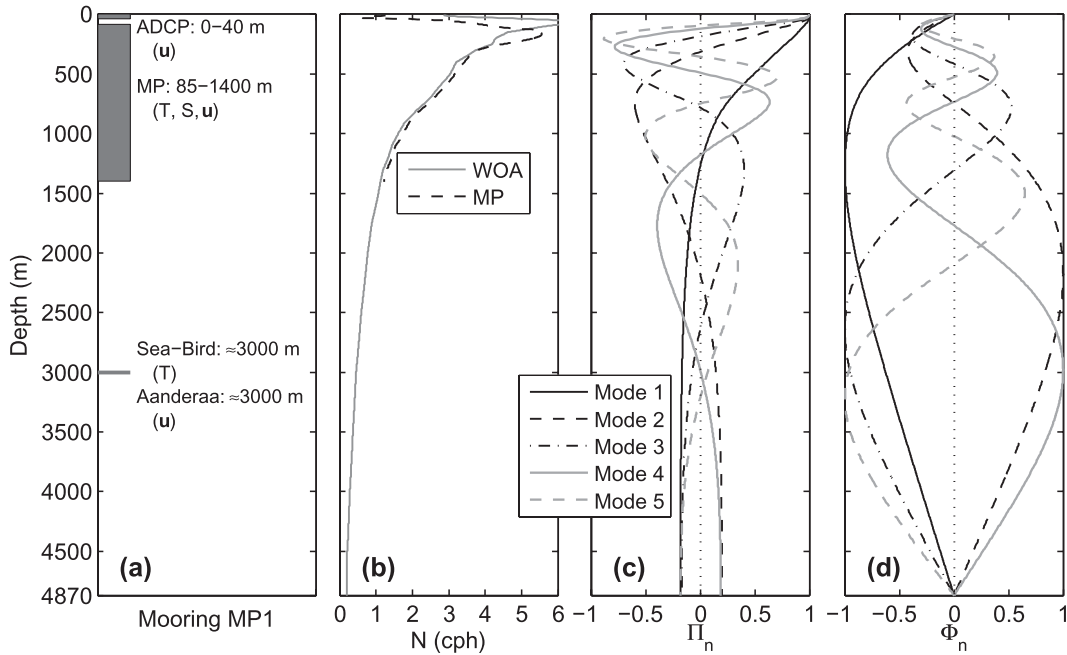


FIG. 2. Mooring instrumentation and ocean stratification profiles at MP1: (a) mooring instruments and measured ocean parameters and (b) buoyancy frequency profiles (in cph). The black line is from the MP measurements. The gray line is from the *WOA05* annual-mean hydrographic data. (c) Normalized vertical structures of the first five baroclinic modes for pressure and horizontal velocity. (d) As in (c), but for vertical displacement and vertical velocity.

and

$$\Phi(z) = -\frac{1}{N^2(z)\rho_0} \frac{d\Pi(z)}{dz}, \quad (3)$$

where ρ_0 is the water density. Here, $N(z)$ is taken from the annual-mean hydrography from *WOA05*. The climatological stratification profile (Fig. 2b, gray) is consistent with the MP measurement (dashed) except in the upper 400 m. This difference has little impact on the modal shapes (Figs. 2c and 2d).

Phase velocity (c_p) and group velocity (c_g) can be derived from the eigenspeed (c_n) following the dispersion relation (Rainville and Pinkel 2006b),

$$c_p = \frac{\omega}{(\omega^2 - f^2)^{1/2}} c_n, \quad (4)$$

and

$$c_g = \frac{(\omega^2 - f^2)^{1/2}}{\omega} c_n, \quad (5)$$

where ω is the M_2 or S_2 tidal frequency and f is the inertial frequency. We will show in section 4b that the

mooring-observed propagation of the semidiurnal internal tide agrees very well with the theoretical values.

The mooring data are highly resolved in the upper 1400 m, equivalent to 62%–68% of the Wentzel–Kramers–Brillouin (WKB) stretched water column (depending on water depth), allowing resolution of the first five modes (Nash et al. 2005). The gaps above and below the ≈ 3000 -m measurements render higher-mode fits unstable in the modal decomposition. Velocity at 3000 m is given a higher weight owing to the longer vertical scales at depth. Error estimates in the modal decomposition are discussed in the appendix.

Five-mode solutions were computed for all moorings except for MP5. At MP5, the failure of ADCP and MP to sample the upper 700 m after 4 days precludes velocity solutions owing to the sensitivity of the velocity fits to the near-surface gaps (Nash et al. 2005). Hence, velocity, energy, and flux results at MP5 are based on the first 4 days alone (preventing separate resolutions of M_2 and S_2). However, mode-1 displacement solutions using deep data alone are stable for the whole time series (due to the location of the mode-1 maximum near 1300 m; Fig. 2d), allowing comparison of moored SSHA with altimetric observations at MP5 as described in section 4. In support of their validity, mode-1 displacements

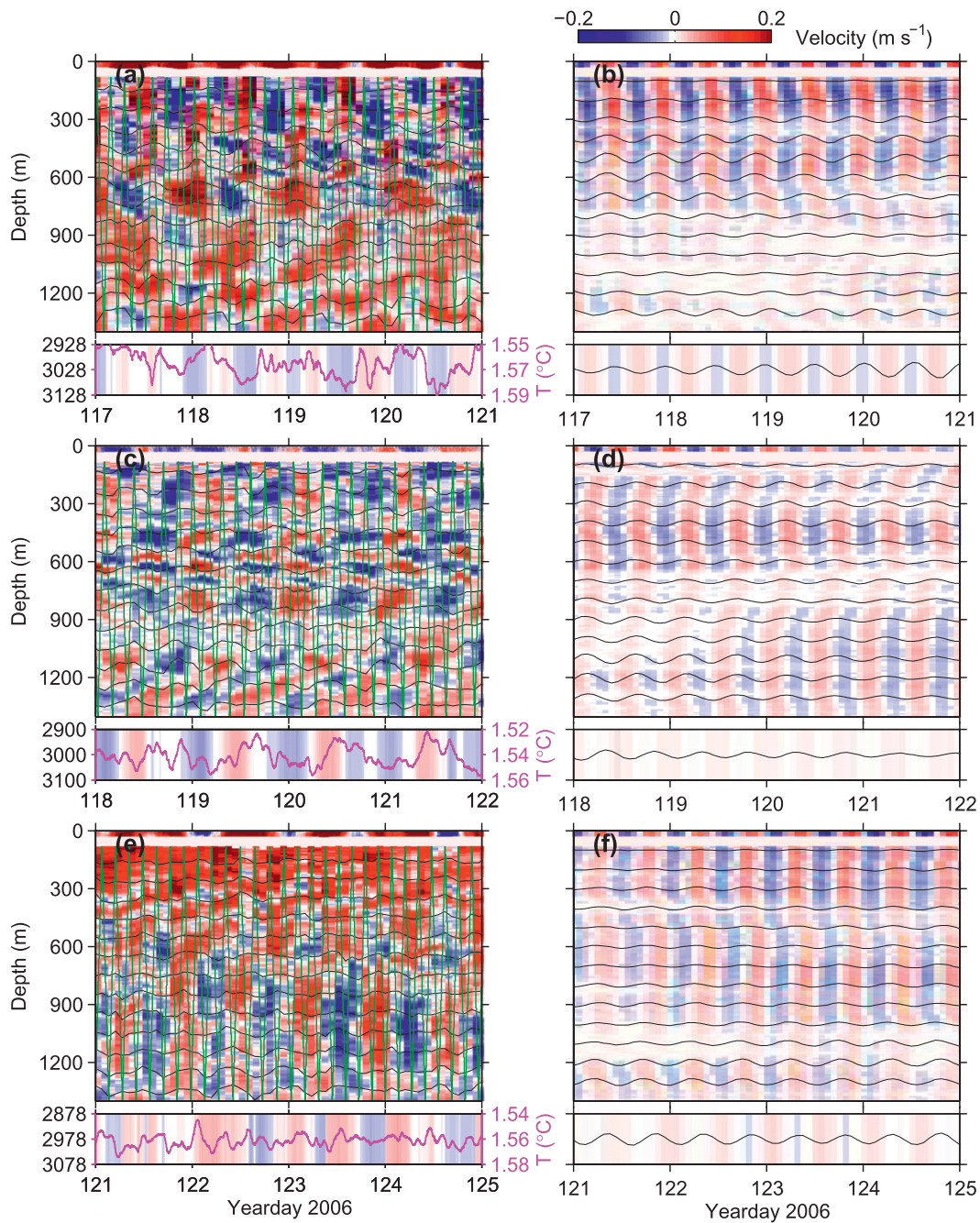


FIG. 3. Samples of (left) raw measurements and (right) bandpassed semidiurnal signals at (a),(b) MP1, (c),(d) MP3, and (e),(f) MP6. Colors indicate along-beam velocities from ADCP (0–40 m), MP (85–1400 m), and Aanderaa (≈ 3000 m), with the scale indicated at the upper right. Pink lines are the Sea-Bird temperature data at ≈ 3000 m depth. Green lines in the left panels show the MP sampling patterns. Isopycnal displacements with mean spacing 100 m are overlotted in black.

computed during the first 4 days using all data and using data deeper than 700 m alone agree well with each other (not shown).

The baroclinic velocity and displacement are expressed as

$$\mathbf{u}'(z, t) = \sum_{n=0}^5 \mathbf{u}'_n(t) \Phi_n(z), \quad (6)$$

and

$$\eta'(z, t) = \sum_{n=1}^5 \eta'_n(t) \Pi_n(z), \quad (7)$$

where $\Phi_n(z)$ and $\Pi_n(z)$ are the vertical structures of the baroclinic modes (Figs. 2c and 2d) and $\mathbf{u}'_n(t)$ and $\eta'_n(t)$ represent the time-varying magnitudes of the baroclinic modes. At each time, $\mathbf{u}'_n(t)$ and $\eta'_n(t)$ are extracted from the velocity and displacement profiles by least squares modal fitting (Alford 2003; Nash et al. 2005). For the velocity, the zeroth-mode, or barotropic, solution is also allowed ($n = 0$).

f. Pressure, SSHA, energy, and flux

These quantities can be calculated for each baroclinic mode independently following the same procedure. For clarity, we neglect the subscript n , which denotes the mode number, in the following equations. Following Nash et al. (2005), the baroclinic pressure perturbation, $p'(z, t)$, is calculated from the modal fit displacement $\eta'(z, t)$ by

$$p'(z, t) = \rho_0 \int_{-z}^0 N^2(\hat{z}) \eta'(\hat{z}, t) d\hat{z} - p^{\text{surf}}(t). \quad (8)$$

The definition of baroclinic motions requires the depth average of the baroclinic pressure perturbation to be zero; therefore, the sea surface pressure, $p^{\text{surf}}(t)$, can be calculated as

$$p^{\text{surf}}(t) = \rho_0 \int_{-H}^0 N^2(z) \eta'(z, t) dz. \quad (9)$$

SSHA caused by the internal tide can be calculated from the sea surface pressure p^{surf} :

$$\text{SSHA} = \frac{p^{\text{surf}}}{\rho_0 g}, \quad (10)$$

where g is the acceleration due to gravity.

Depth-integrated horizontal kinetic energy and available potential energy are computed from the above modal fit baroclinic perturbations, $\mathbf{u}'(z, t)$ and $\eta'(z, t)$, by

$$\text{HKE} = \frac{1}{2} \rho_0 \int_{-H}^0 \langle |\mathbf{u}'(z, t)|^2 \rangle dz, \quad (11)$$

and

$$\text{APE} = \frac{1}{2} \rho_0 \int_{-H}^0 \langle N^2(z) \eta'^2(z, t) \rangle dz, \quad (12)$$

where the angle brackets indicate the average over one tidal cycle. The total energy E is calculated by

$$E = \text{HKE} + \text{APE}. \quad (13)$$

The depth-integrated energy flux is computed as the covariance of the modal fit velocity and pressure perturbations by

$$\mathbf{F} = \int_{-H}^0 \langle \mathbf{u}'(z, t) p'(z, t) \rangle dz. \quad (14)$$

g. Coherent portion

For each mode, the bandpassed semidiurnal internal tide is further decomposed into coherent and incoherent constituents. Neglecting the much weaker N_2 and K_2 constituents, coherent M_2 and S_2 signals are harmonically fit using tide analysis software (Pawlowicz et al. 2002). Because both the modal fitting and harmonic fitting operations are linear, their order makes no difference. We chose to conduct harmonic analyses on the modal fits.

The baroclinic velocity and pressure signals are thus expressed as

$$(\mathbf{u}', p')_{\text{semi}} = (\mathbf{u}', p')_{M_2} + (\mathbf{u}', p')_{S_2} + (\mathbf{u}', p')_{\text{in}}, \quad (15)$$

where $(\mathbf{u}', p')_{\text{in}}$ represent the incoherent constituents.

For each constituent, the energy and flux are calculated following the procedure described in section 2f. According to Eq. (14), the coherent flux is calculated as

$$\begin{aligned} \langle \mathbf{u}'_{(M_2+S_2)} p'_{(M_2+S_2)} \rangle &= \langle \mathbf{u}'_{M_2} p'_{M_2} \rangle + \langle \mathbf{u}'_{S_2} p'_{S_2} \rangle \\ &+ \langle \mathbf{u}'_{M_2} p'_{S_2} + \mathbf{u}'_{S_2} p'_{M_2} \rangle. \end{aligned} \quad (16)$$

The first and second terms are the M_2 and S_2 fluxes, respectively. The two cross terms between M_2 and S_2 lead to the spring-neap cycles. If averaged over an integer number of spring-neap cycles (≈ 14.7 days), the cross terms will cancel.

The coherent fractions (CFs) comprising the energy and flux magnitude are then computed for each mode as

$$\text{CF}^E = \frac{E_{(M_2+S_2)}}{E_{\text{total}}}, \quad (17)$$

and

$$\text{CF}^F = \frac{|F|_{(M_2+S_2)}}{|F|_{\text{total}}}. \quad (18)$$

This definition is straightforward for energy. However, because flux is a vector quantity, the definition for flux overestimates the coherent fraction in its exclusion of variations in direction. That is, signals with constant magnitude but wandering angle would give $\text{CF}^F = 1$.

It is known that record length affects the partitioning between incoherent and coherent signals. The record lengths of MP1, MP2, MP3, and MP6 range between 40 and 50 days, while the MP4 time series is only 23 days. The definition of a coherent fraction in this manner may cause confusion. That is, incoherent signals owing to fluctuations in amplitude and phase on time scales longer than the deployment time are not distinguishable as such. This will be kept in mind when comparing coherent signals from the mooring data (≈ 2 months) and the T/P altimeter data (≈ 10 yr).

h. Altimeter data and methods

The IWAP mooring array lies directly under T/P track 249 (Fig. 1, black dots and line). In section 4a, the altimetric results along track 249 will be compared with moored results. Altimetric SSHA is computed following the work of Zhao and Alford (2009), which employs data from both the T/P original tracks and tandem tracks, resulting in higher spatial resolution (≈ 250 km). Briefly, along-track SSHA data spanning 1993–2005 are processed with standard corrections for instrumental bias, environmental effects, and the barotropic tide (Ray 1999; Berwin 2003b). Along each track, data are resampled onto a 6.2-km spatial grid (Berwin 2003a), and bandpass filtered with spatial cutoffs of (120, 400) km to isolate the mode-1 internal tide (≈ 160 km in our region).

The M_2 and S_2 signals in the T/P SSHA time series have alias periods of 62.1 and 58.7 days, respectively. They can be extracted by harmonic analysis at each location (e.g., Ray and Mitchum 1996; Cummins et al. 2001). In our technique, harmonic analysis is used to solve for traveling solutions over a range of spatial locations, enabling separate resolutions of the northward and southward components. Multiple internal tide wave trains can then be resolved by plane-wave fits using data from all tracks in a fitting region, at the expense of the spatial resolution (Zhao and Alford 2009). Here, we choose the fitting region to be $250 \text{ km} \times 250 \text{ km}$ on an overlapping grid of $0.1^\circ \times 0.1^\circ$. Internal tidal beams from the Aleutian Ridge and Hawaiian Ridge are successfully separated (section 5).

3. Mooring-observed internal tides

We here present the internal tides as observed in the mooring array using these techniques. We begin with the spatial pattern of the time-mean flux (section 3a), then present time series of velocity, displacement, energy, and flux at several sites north of the Hawaiian Ridge (section 3b). These measurements show the relative contributions of higher-mode and incoherent signals.

a. Time-mean flux

As seen in Fig. 1 (red arrows) and noted by Alford et al. (2007), observed semidiurnal energy flux is generally aligned along a beam toward $\approx 60^\circ$, apparently emanating from FFS, as indicated by numerical simulation (yellow arrows). The flux generally decreases moving northeastward, $\approx 3.5 \text{ kW m}^{-1}$ at MP1 and $\approx 1.2 \text{ kW m}^{-1}$ at MP6 (Table 1), but not monotonically. An example is MP4, whose flux is about twice that of MP3, and more eastward than at other locations. As will be shown below (section 5), the general nonmonotonicity, and the specific magnitude and direction of the MP4 flux, are consistent with an interference pattern formed by the northeastward Hawaiian and southeastward Aleutian beams.

b. Progression through the profiler array

To gain a qualitative sense of the internal tide as a function of distance from the source, time series for MP1, MP3, MP4, and MP6 are presented (Figs. 4–7). The plot format will be presented for MP1, followed by discussion of the other sites.

1) INTERNAL TIDE AT MP1

The internal tide is clearly visible at MP1, only 218 km from its primary generation region near FFS, as three successive periods of more intense velocities (Figs. 4a and 4b, colors) and greater displacements (black lines), separated by more quiescent periods. These bandpassed semidiurnal signals are a combination of M_2 , S_2 , and incoherent constituents, as indicated earlier. A variety of vertical wavelengths can be discerned in the velocity (Fig. 4a). Nonetheless, modal decomposition indicates a dominance of mode 1 (Fig. 4c), as seen qualitatively in the top panel of Fig. 4 with deep flows measured at the Aanderaa site generally opposing those at shallower depths. In addition, velocity weakens appreciably approaching the mode-1 node near 1300 m (refer to Fig. 2c). Stronger mode-2 signals are seen in the displacement (Fig. 4d). However, the energy and flux are still dominantly mode 1 (Figs. 4g and 4h).

The consistency among the observed signals with a theoretical free-propagating wave northeastward along the array is examined next via two forms of hodographs, following Alford and Zhao (2007a). Such a wave would be expected to show current ellipses elongated in the along-beam direction (Fig. 4e, black), and along-beam velocity v' in phase with η , with the slope indicated (Fig. 4f, black). Elongation of observed ellipses, which are computed in evenly spaced windows spanning the time series, varies with time but is not generally aligned with that expected for an along-beam free wave. However, the $v'\eta'$ ellipses are in excellent agreement with a northeastward

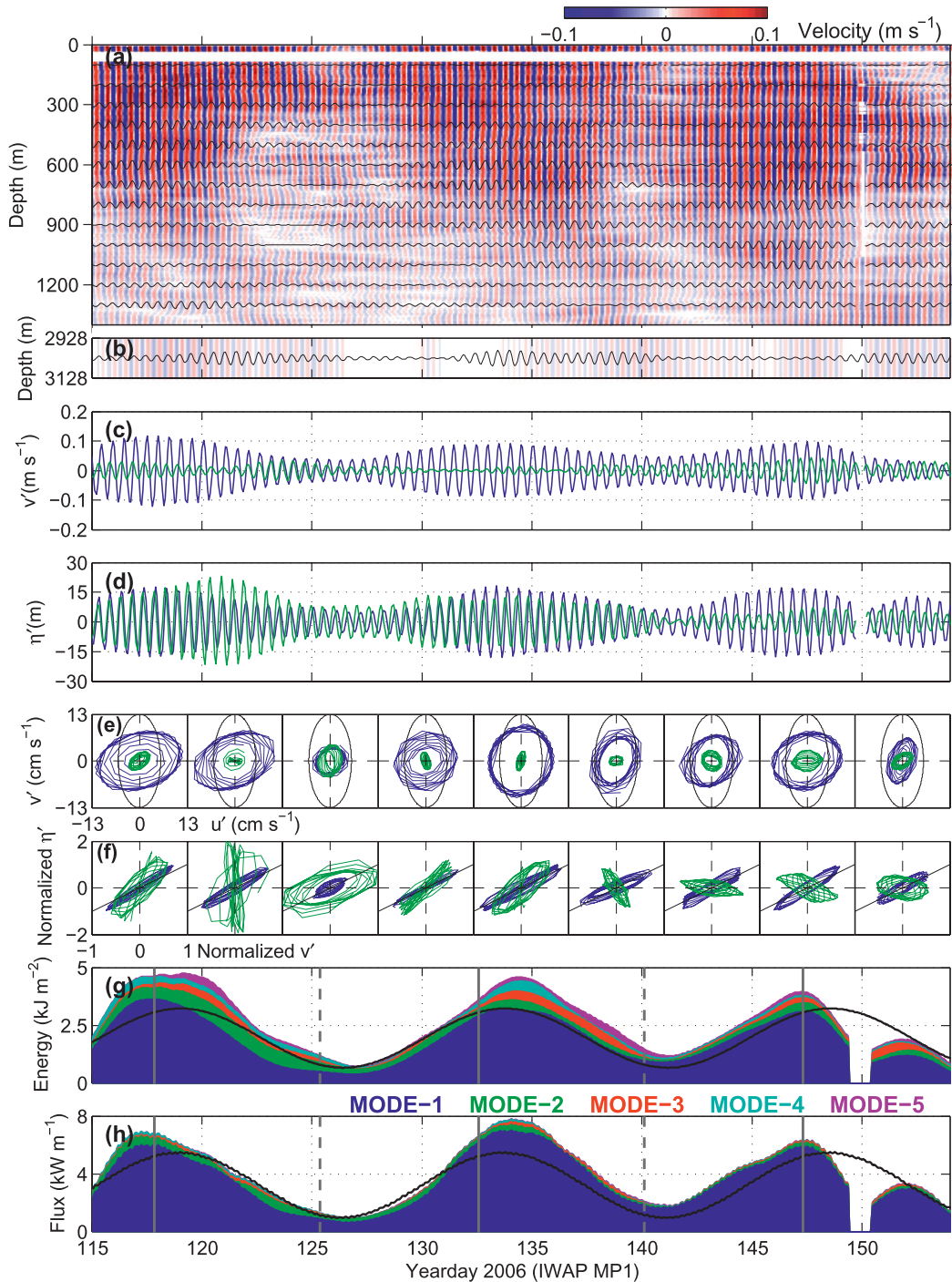


FIG. 4. Time series of the semidiurnal internal tide at MP1. (a) Semidiurnally bandpassed along-beam velocity (colors) and isopycnal displacement (black lines) from the ADCP and MP measurements. (b) As in (a), but for the Aanderaa and Sea-Bird measurements at ≈ 3000 m depth. Black lines indicate isothermal displacement rather than isopycnals. (c) Along-beam velocity amplitude for modes 1 (purple) and 2 (green). (d) As in (c), but for vertical displacement. (e) The $u'v'$ hodographs of the mode-1 (purple) and -2 (green) components. The black ellipsis is for a theoretical free wave propagating northeastward along the beam. (f) As in (e), but for $v'\eta'$ hodographs. Normalization is such that a free wave propagating along the beam would fall along the black line. (g) Energy in modes 1–5 (stacked colors) and the coherent $M_2 + S_2$ constituent of the sum of the first five modes. (h) As in (g), but for flux magnitude. In (g) and (h), times of spring and neap barotropic tides at FFS (map refer to Fig. 1), predicted from the TPXO6.2 tidal model, are shown as vertical solid and dashed lines, respectively.

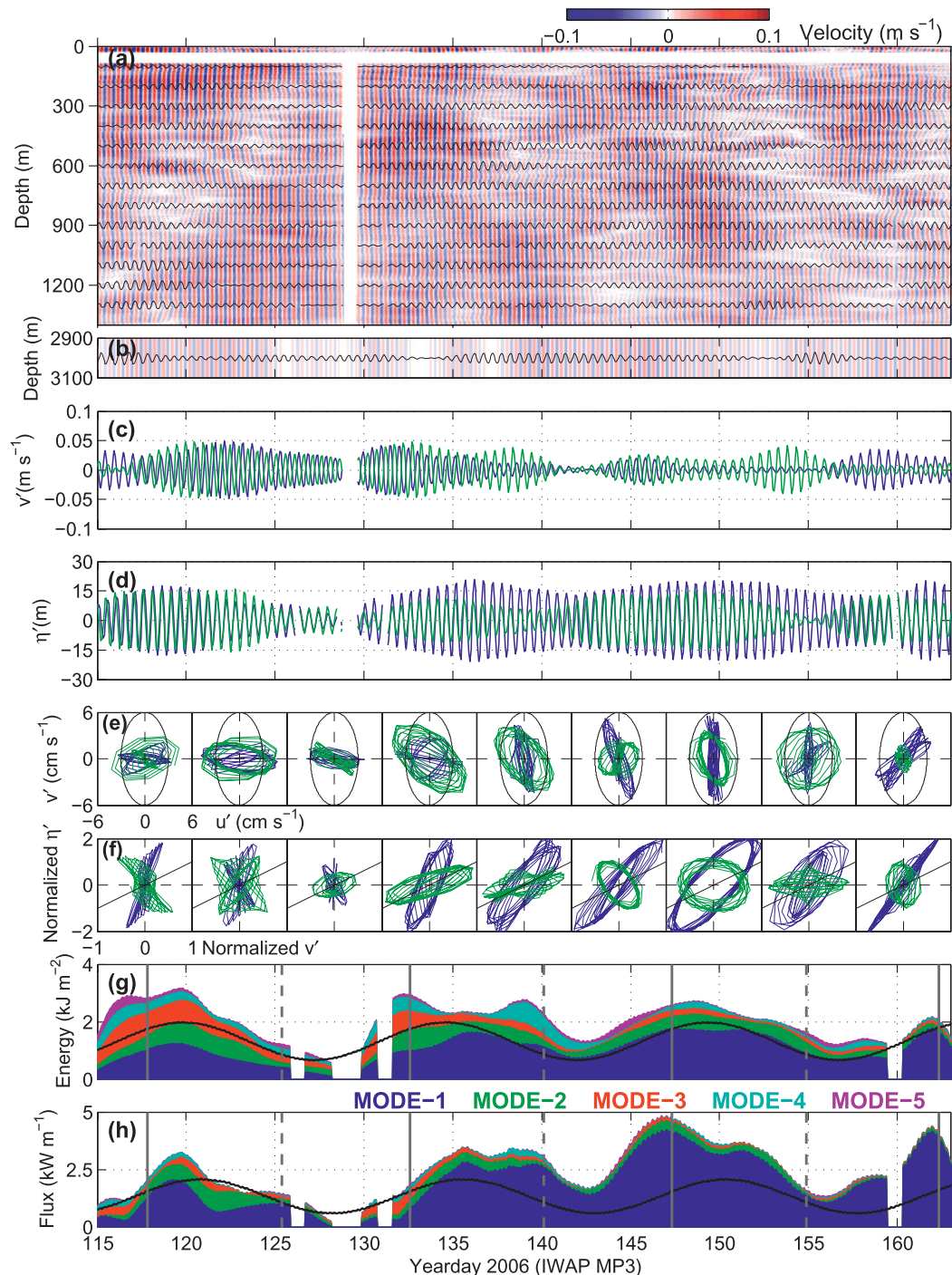


FIG. 5. As in Fig. 4, but for MP3.

free wave for mode 1 (Fig. 4f, blue). Taken together, these indicate interference between the signals generated at FFS to the east and Brooks Banks (BB) to the west (Fig. 1): the along-beam velocity would still be expected to be in phase with the displacement, but the two sources lead to distorted $u'v'$ ellipses relative to that

for a single wave. That is, ellipses are not necessarily aligned with flux vectors in a multidirectional wave field (K. I. Martini et al. 2010, unpublished manuscript). Mode-2 hodographs are more variable (Fig. 4f, green), and even consistent with southward propagation toward the end of the record.

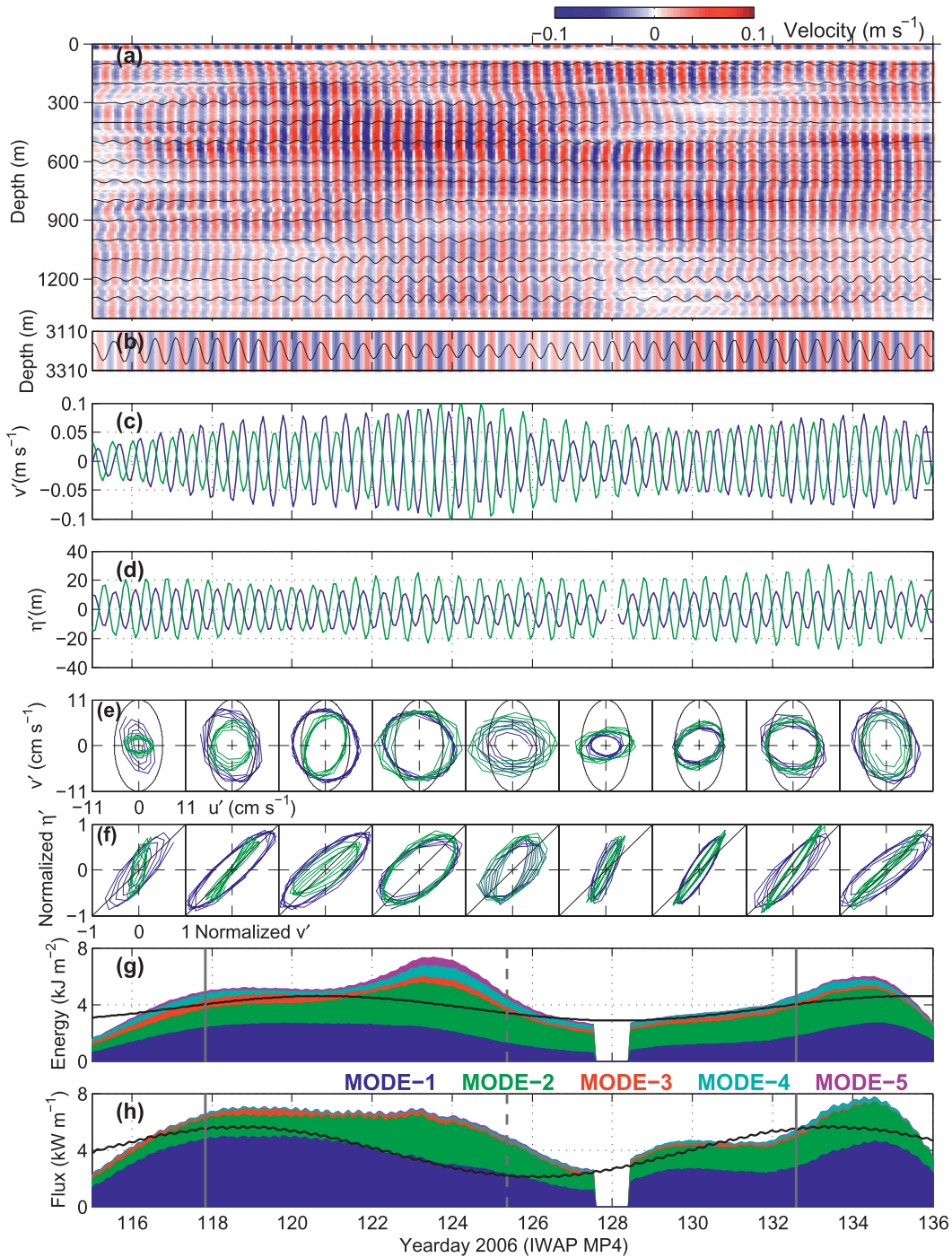


FIG. 6. As in Fig. 4, but for MP4.

The energy (Fig. 4g) and flux magnitude (Fig. 4h), plotted as stacked bands colored by mode, show clear spring–neap cycles dominated by mode 1 (even more so for flux than for energy). The spring–neap cycles in the energy and flux are synchronous, with spring-tide values exceeding neap-tide values by a factor of about 5. For MP1,

the signals are strongly coherent and, hence, the semidiurnal flux and energy vary only slightly from the sum of the coherent portion of the first five modes (heavy black). The 0.7-day time lag of springs and neaps relative to the semidiurnal tidal forcing at FFS (24°N, 193.5°E) (Figs. 4g and 4h, gray and dashed lines, respectively) is consistent with

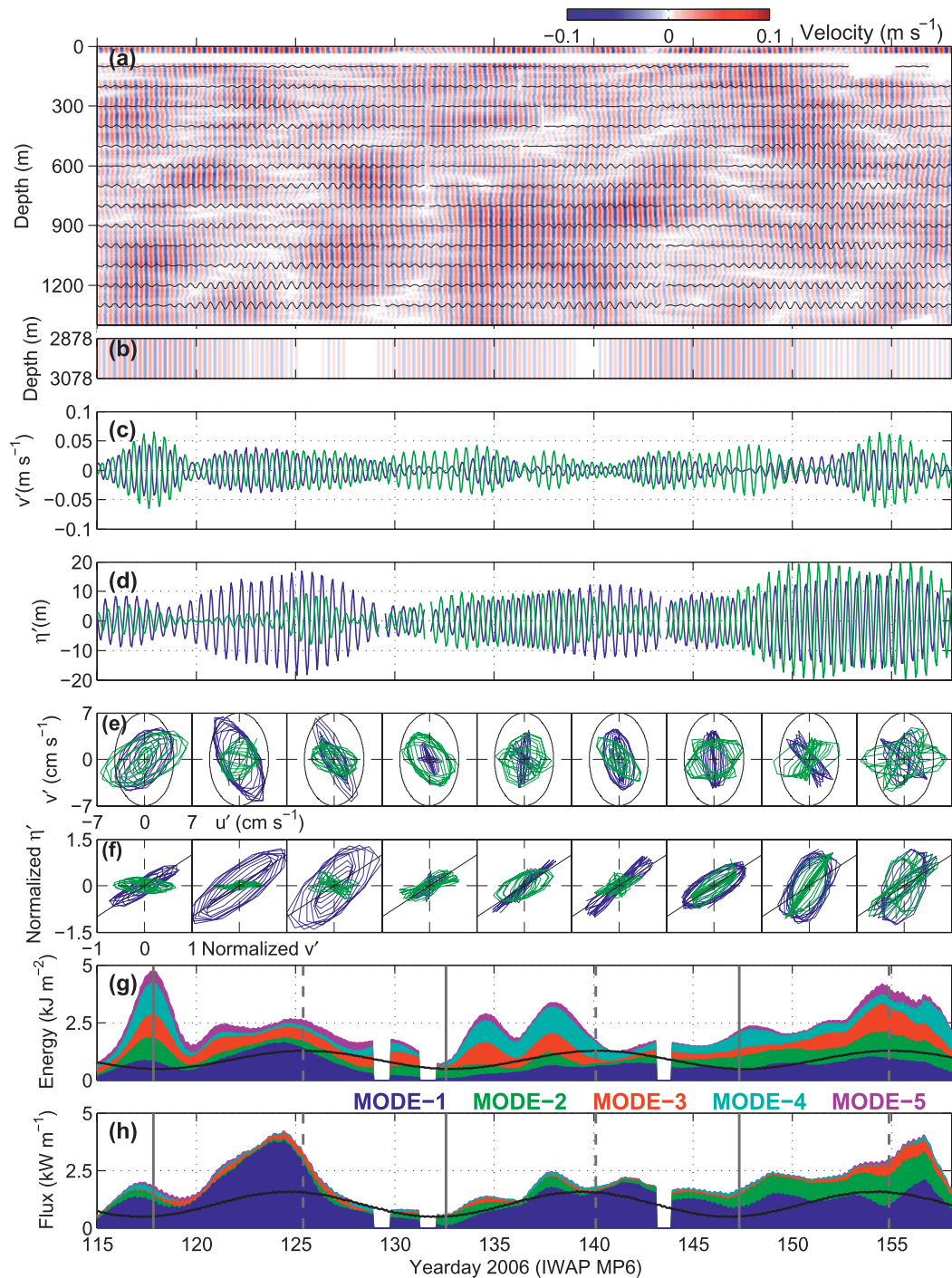


FIG. 7. As in Fig. 4, but for MP6.

the group propagation expected for the mode-1 tide, as found by Alford and Zhao (2007a) and shown in more detail later (section 4b).

To summarize, the various signals at MP1 are as expected given its proximity to the forcing regions; namely,

they indicate a largely coherent mode-1 tide propagating northeastward at the expected rate. Hodographs indicate interfering northeastward radiation from multiple sources at the Hawaiian Ridge. Southward signals are detected in mode 2, but are weak or undetectable in mode-1 flux.

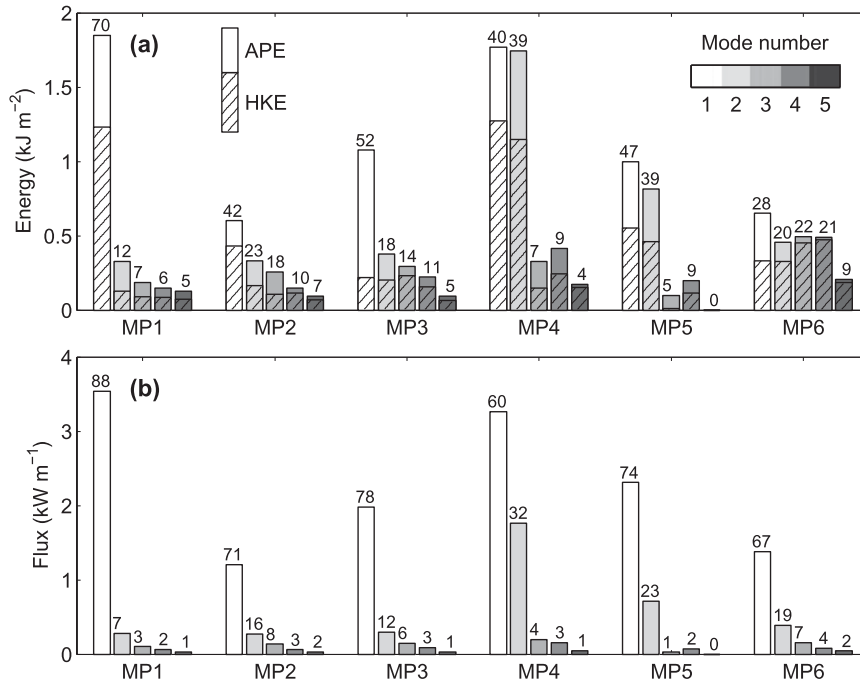


FIG. 8. Modal partition of (a) energy and (b) flux of the semidiurnal internal tide. The percentage of each mode is given at the top of the bar. In (a), APE and HKE are distinguished with different hatching patterns.

2) ALONG-BEAM VARIATIONS

Moving northeastward, moored measurements are displayed in the same format for MP3, MP4, and MP6 (Figs. 5–7).

In contrast to the strong visual dominance of low-mode signals at MP1, higher-mode signals grow in importance moving away from the source. Mode-1 and -2 amplitudes are comparable at each site for both velocity and displacement (panels c and d in Figs. 5–7). These lead to greater contributions in the higher-mode energy (panel g in Figs. 5–7). However, the flux (panel h in Figs. 5–7) continues to be dominated by mode 1 at all sites owing to the red vertical wavenumber spectrum for the baroclinic pressure, as found previously (Alford 2003; Nash et al. 2005).

These conclusions are seen in a more quantitative comparison of the modal content for the energy (Fig. 8a) and flux (Fig. 8b). The modal content for the energy changes from a strong mode-1 dominance at MP1 to near equipartition at MP6, consistent with a decaying mode-1 wave superimposed on a white vertical wavenumber background.

MP4 stands out for its strong mode-2 contribution. The lag of the spring-tide peaks for mode 2 is consistent with travel time from Hawaii, but the short record prevents drawing a stronger conclusion. Local generation near the Musicians Seamounts is also a possibility (refer

to Fig. 1). Still, the greatest flux is mode 1 as seen in the time series.

The partitioning between HKE and APE (Fig. 8, plain and hatched boxes) also varies along the array. For a free-propagating internal tide, HKE always exceeds APE in a latitude-dependent ratio ranging from 1.5 at MP1 to 2.3 at MP6, following

$$\frac{\text{HKE}}{\text{APE}} = \frac{\omega^2 + f^2}{\omega^2 - f^2}, \tag{19}$$

where ω is the tidal frequency and f is the inertial frequency. The observed ratio at MP1 is ≈ 2 , generally consistent with a free progressive wave. However, in contrast to these free-wave values, the observed APE exceeds HKE at MP3, MP5, and MP6, implying standing-wave patterns (Alford and Zhao 2007a; Zhao and Alford 2009). Additionally, the interference between multiple internal tidal beams is evidenced by the more eastward flux seen at MP2–MP4. As will be shown in section 5, these moorings are influenced by the southeastward Aleutian internal tide, as well as by the northeastward Hawaiian beam.

Coherence with astronomical tidal constituents as defined above generally decreases with increasing range (Fig. 9). (The increased coherence at MP4 is a consequence of its shorter record length.) In contrast to the visually apparent spring–neap cycles in the velocity and displacement at MP1, these are less obvious at the more

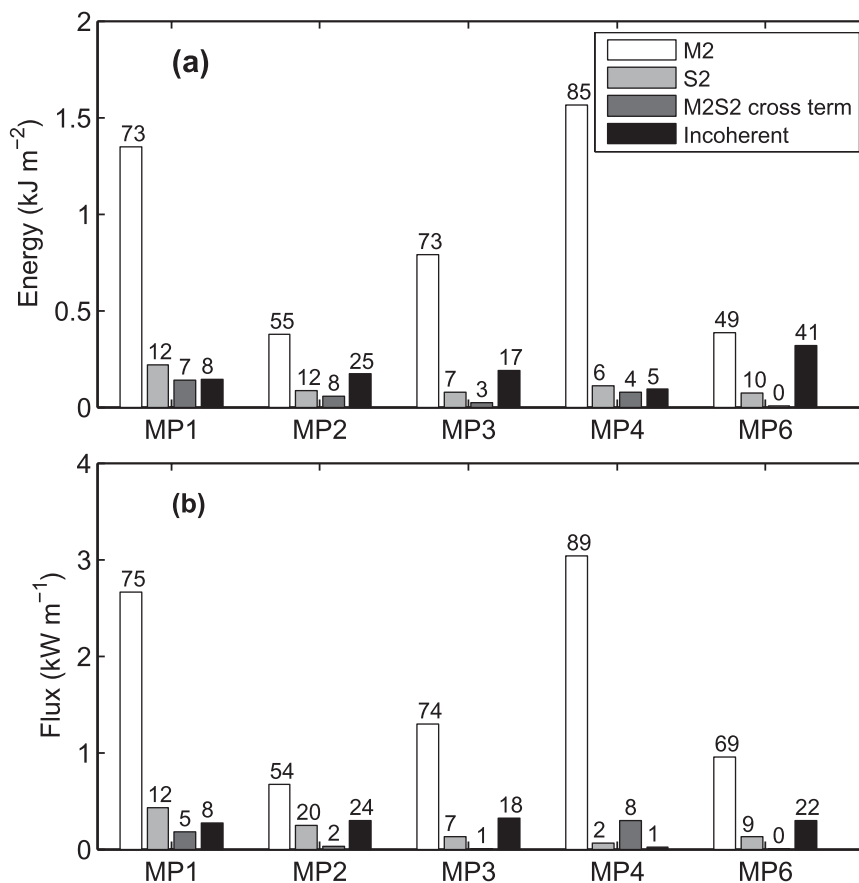


FIG. 9. (a) Energy and (b) flux of the mode-1 semidiurnal internal tide. The bandpassed semidiurnal internal tide is divided into four constituents: M_2 , S_2 , the M_2S_2 cross term, and the incoherent constituent. Their percentages are given at the tops of the bars.

northern sites partially owing both to amplitude and phase variations in the low-mode solutions (panels c and d in Figs. 5–7) and to greater contributions from less-coherent higher modes. Spring–neap cycles in energy and flux are still evident at MP3 and MP6 (the record at MP4 is too short for certainty), but the growing incoherence is evident as an increasing difference between the coherent (panels c and d in Figs. 5–7, black line) and total quantities (colors).

In summary, our observations indicate a rich time-variable multimodal internal tide field. Hodographs suggest that the internal tides radiated from multiple Hawaiian sources, rather than a single-point source at FFS, in addition to contributions from the Aleutian Ridge that will be examined in the following sections. Incoherence with astronomical tidal forcing can arise from variations in amplitude at generation (Mitchum and Chriswell 2000; Chriswell 2002) and refraction in eddy field (Rainville and Pinkel 2006b). Still, the bulk of the time-mean energy flux is carried by the coherent mode-1 internal tide, warranting its separate consideration next.

4. Comparisons with altimetric observations

We next conduct a direct comparison of the moored and altimetric SSHAs, taking advantage of the collocation of the IWAP mooring array and T/P track 249 (Fig. 1). We here focus on the mode-1 semidiurnal internal tide, because it carries the bulk of the tide energy, and because it is by far the most easily detectable in the altimetric measurements. The moored mode-1 SSHA is extracted by projecting profiles of mooring measurements onto discrete baroclinic modes as described in section 2e. The altimetric mode-1 SSHA is extracted by harmonic analysis and the new south–north separation technique (section 2h).

a. Moored and altimetric SSHA

For the most basic comparison, at each mooring site, the moored semidiurnal SSHA from the bandpass filter is plotted (Fig. 10, gray line) with the sum of the harmonic-fit altimetric M_2 and S_2 SSHA signals (black line). The altimetric records show the spring–neap beating of the

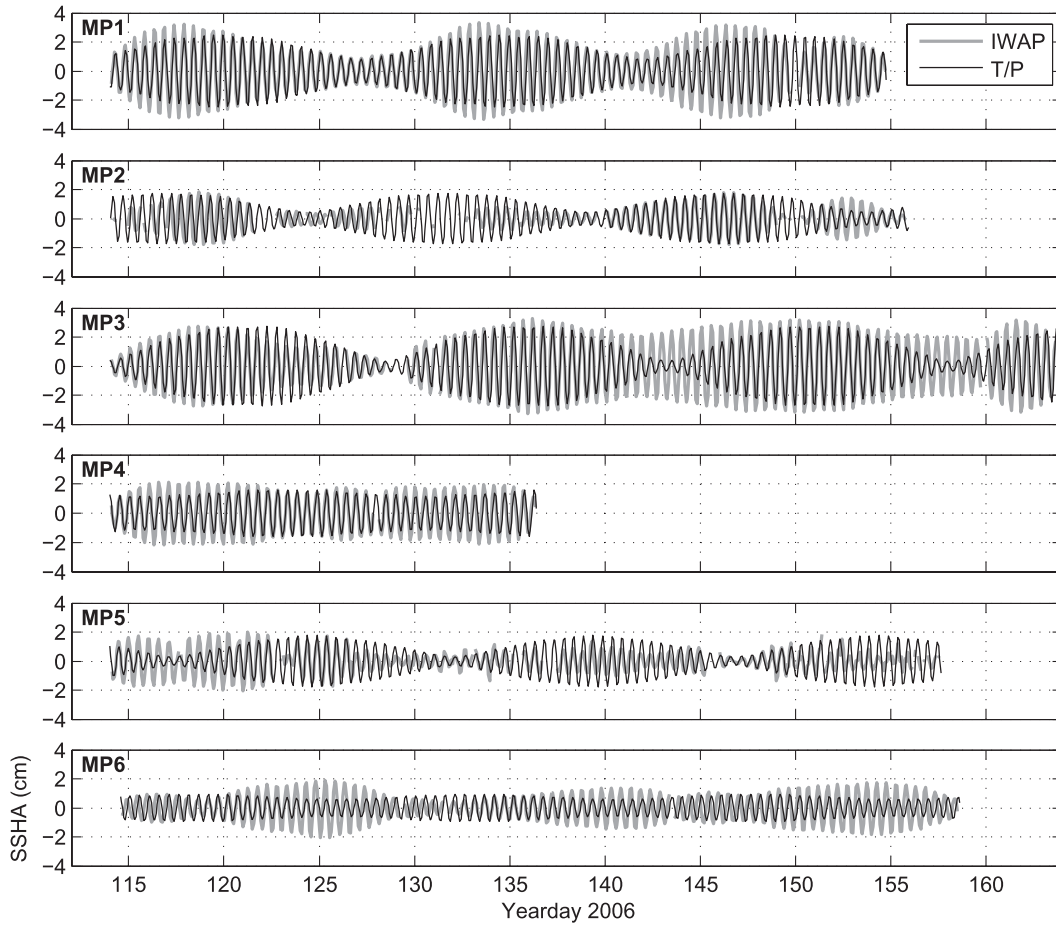


FIG. 10. Comparison of the moored and altimetric mode-1 baroclinic SSHAs. The gray lines are the bandpassed semidiurnal signals from the IWAP moorings. The black lines are the $M_2 + S_2$ constituents extracted from the T/P altimeter data along track 249.

M_2 and S_2 constituents. In contrast, the temporally variable incoherent signal is also seen in the moored time series. In spite of this, a remarkable degree of agreement in magnitude and phasing is seen between the in situ and remotely sensed data as far north as MP5. Amplitude and phase differences finally develop at MP6 (≈ 1600 km from FFS).

For a more direct comparison, the amplitude and phase of the harmonically fit signals are compared for M_2 and S_2 (Fig. 11). The moored harmonic fits are extracted in overlapping windows of 14.7 days (a spring-neap tidal cycle); then, the mean and standard deviation are plotted as dots and bars, respectively. As described in section 2h, altimetric signals are harmonically extracted for the northward (red) and southward components (green), and the total (black). For M_2 , the total SSHA shows general (but nonmonotonic) northeastward decay, and half-wavelength modulation of amplitude indicative of a partial standing wave resulting from superposed signals from Hawaii and the Aleutians

(Zhao and Alford 2009), as examined in detail below. The northward-southward-separated components (red and green) both show almost linearly increasing phase. For S_2 , the differences are somewhat larger due in part to its weaker signals; however, interference between northward and southward signals is still discernible, as shown in the separated components (Figs. 11c and 11d, red and green).

Moored and altimetric M_2 signals are in good agreement in both amplitude and phase, in spite of the greatly different bandwidths of the two coherent estimates (≈ 2 months versus ≈ 10 yr). Some of the differences are explainable in terms of the different time scales affecting the two estimates. That is, the altimetric estimates are the signals that are time invariant over a 10-yr record. In contrast, processes such as mesoscale eddies and annual cycles lead to differences in both generation (Mitchum and Chriswell 2000) and propagation time (Rainville and Pinkel 2006a). For example, a greater moored amplitude at MP3 may be due to stronger generation during the

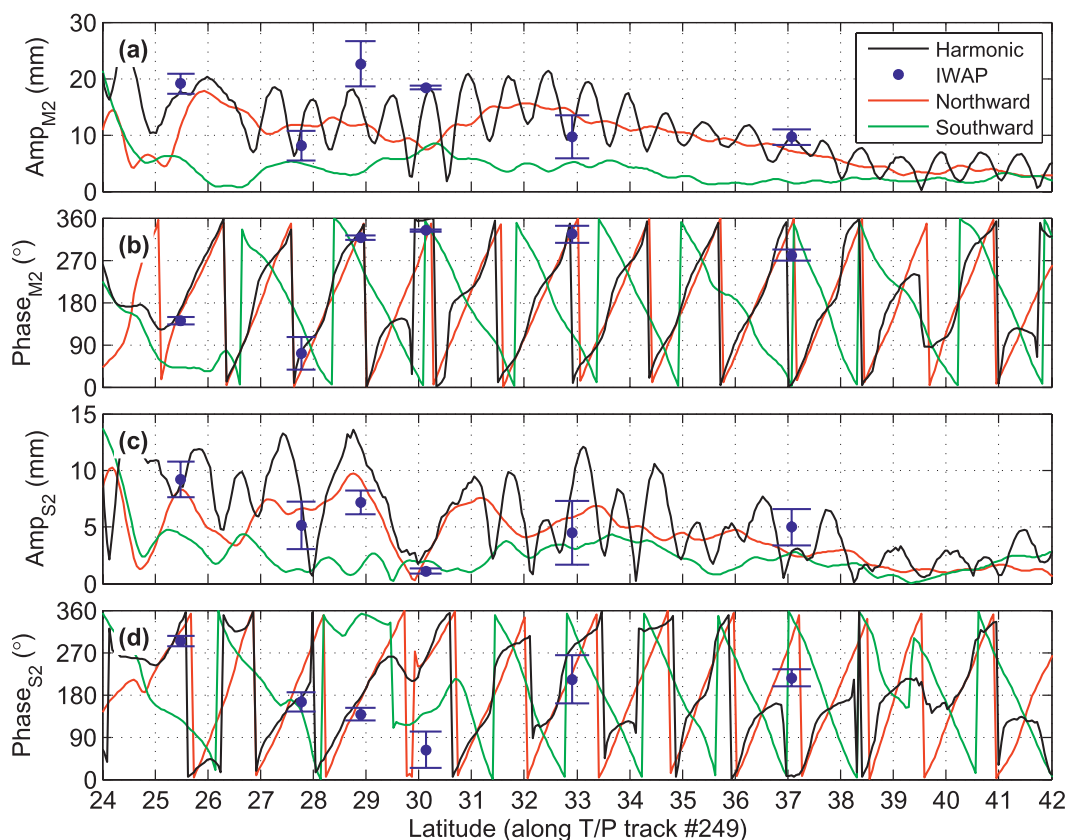


FIG. 11. Comparison of the moored and altimetric mode-1 baroclinic SSHAs. (a),(b) Amplitude and phase of the M_2 SSHA. The black lines are the harmonically extracted SSHA signals along T/P track 249. The red and green lines indicate the northward and southward components of the altimetric SSHA, respectively. The purple dots and bars represent the means and standard deviations of the IWAP moored SSHA. The reference time is 0000 UTC 1 Jan 1992. (c),(d) As in (a),(b), but for the S_2 SSHA.

time of the IWAP measurements owing to variations in thermocline depth. Alternately, refraction could have shifted the antinode in the interference pattern closer to MP3 during this period. At MP6, the moored and altimetric phases differ by $\approx 70^\circ$, which is too large to be explained by the 43-km spatial offset (Table 1), which is parallel to wave crests (Fig. 1). We speculate that refractive phase shifts during the time of the IWAP deployment relative to the longer-term altimetric mean may be responsible.

b. Spatial propagation

The northeastward progression of the mode-1 semi-diurnal internal tide at phase and group speeds is now examined. Theoretical propagation times are first computed for a linear free wave propagating toward the northeast by integrating Eqs. (4) and (5) along the mooring array starting from FFS (Fig. 1), following previous work (Rainville and Pinkel 2006b; Alford and Zhao 2007a). Travel time is plotted versus latitude with dashed lines in Figs. 12a–c, with the associated speeds

given in Fig. 12d. Phase travel times for M_2 (Fig. 12a) and S_2 (Fig. 12b) are nearly indistinguishable from one another. However, the slight difference between their implied wavelengths leads to dispersion and group propagation (Fig. 12c).

For the altimetry, the phase propagation time is calculated by unwrapping phases of the northward M_2 and S_2 SSHAs, each of which increases northward along the track (Figs. 11b and 11d, red line). To focus on the signals emanating from Hawaii, only the northward component is used.

Our separate resolution of the M_2 and S_2 enables an altimetric estimate of group propagation (Fig. 13), which to our knowledge has not been attempted. Group propagation of the coherent signals arises from the phase difference between M_2 and S_2 . Note that the phase propagation times of M_2 and S_2 have very slight differences (Figs. 12a and 12b, gray line). The M_2 and S_2 phases (Fig. 13a) diverge owing to their different wavelengths, as is better seen in the unwrapped quantity (Fig. 13b). Their phase difference and a linear fit are shown in gray and

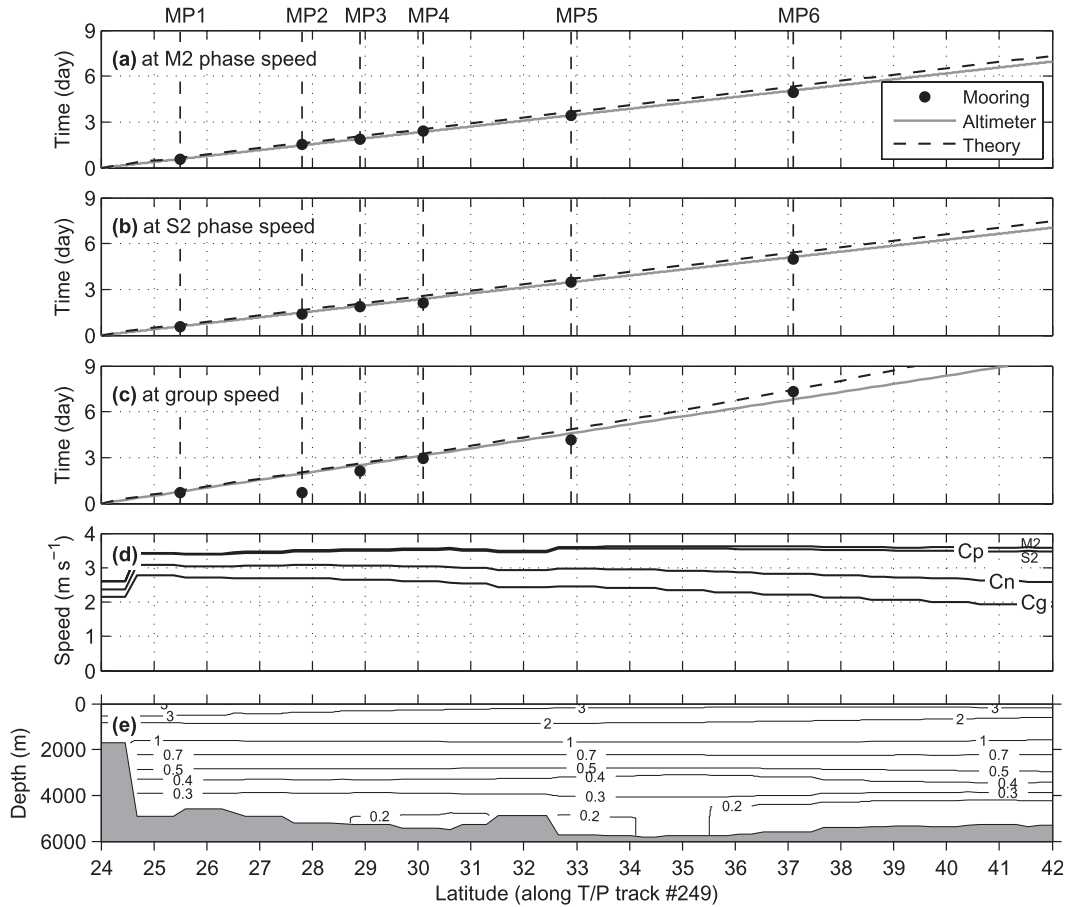


FIG. 12. Propagation of the mode-1 semidiurnal internal tide along the IWAP mooring array and T/P track 249 (refer to Fig. 1). (a) Propagation time at the M_2 phase speed, calculated from moorings (dots), T/P altimeter data (gray), and theory (dashed). (b) As in (a), but for propagation time at the S_2 phase speed. (c) As in (a), but for propagation time at the group speed. (d) Theoretical eigenspeed c_n , group speed c_g , and phase speeds (c_p) of M_2 and S_2 . (e) Buoyancy frequency contour (in cph) from WOA05.

black, respectively, in Fig. 13c. The spring and neap tides appear at the spatial locations where M_2 and S_2 are in phase ($\Delta\phi = 0^\circ$) and out of phase ($\Delta\phi = 180^\circ$), respectively. For the chosen reference time 0000 UTC 1 January 1992, the spring tide occurs at 40.4°N , and the neap tide at 26.3°N . The distance (≈ 1740 km) divided by the time (≈ 7.4 days, half of a spring–neap tidal cycle) gives a mean group velocity of ≈ 2.7 m s⁻¹, which is in line with theoretical values (Fig. 12d).

For the moorings, the M_2 and S_2 phase propagation times are computed (Figs. 12a and 12b, dots) by integrating phases of the M_2 and S_2 SSHAs, respectively (Figs. 11b and 11d, purple dots). Because the moored phase estimates may have an integral number of tidal periods added to them, the altimetric phase (which agrees well with the moored phase; Figs. 11b and 11d) is used to resolve this uncertainty. A group propagation time (Fig. 12c, dots) is estimated from the time lag of the observed spring–neap maxima in the energy flux at each

mooring (Figs. 4–7), relative to those in the barotropic forcing at FFS, following Alford and Zhao (2007a). At MP5, SSHA rather than flux is used, because the flux time series is too short to have spring–neap cycles (section 2e).

In summary, the phase and group estimates computed from moorings and altimetry agree well with each other, and with expectations from linear theory. The moored group speed estimate for MP2 is an exception, probably because of a noisy and less well pronounced spring–neap cycle (not shown).

5. Interference patterns

Several observations reported in the previous sections imply an interference pattern that results from multiple superposed waves: 1) eastward deflection of the moored time-mean energy flux at MP2–MP4 rather than at MP1 (Fig. 1); 2) variation of the HKE/APE ratio,

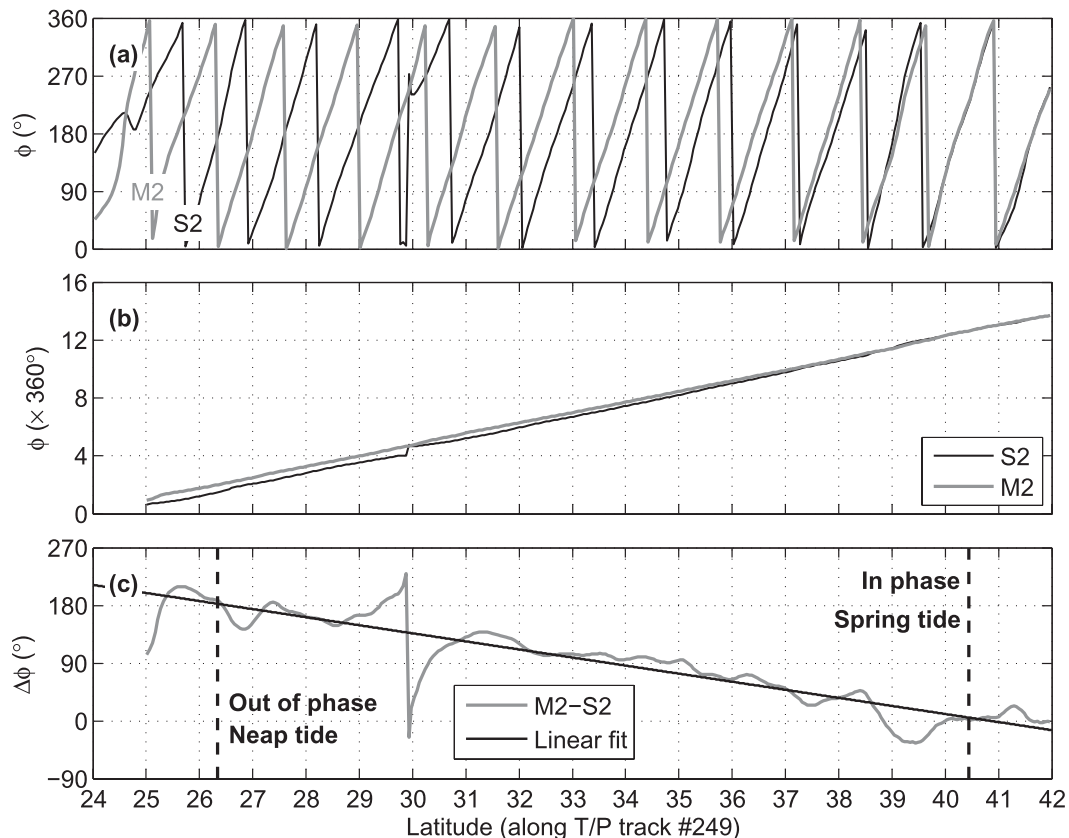


FIG. 13. Spatial dependence of spring and neap tides observed from the T/P altimeter data along track 249. (a) Phase of the northeastward M_2 and S_2 internal tides. The reference time is 0000 UTC 1 Jan 1992. (b) As in (a), but for the unwrapped phase. (c) Phase difference between the M_2 and S_2 constituents (gray) and its linear fit (black). At 26.3°N, M_2 and S_2 are out of phase ($\Delta\phi = 180^\circ$), indicating a neap tide. At 40.4°N, M_2 and S_2 are in phase ($\Delta\phi = 0^\circ$), indicating a spring tide.

which varies in contrast to the constant value for a single progressive wave (Fig. 8); and 3) half-wavelength amplitude modulations in altimetric SSHA, and their separate resolution into north and south components (Fig. 11). Here, we employ the altimetry and a simple two-wave model to further examine the internal tide field in a two-dimensional view, instead of the above one-dimensional picture along the mooring array. We will show that the IWAP moorings lie in the overlapping region of northeastward Hawaiian and southeastward Aleutian fluxes. Our focus is on the dominant M_2 internal tide, though S_2 also shows standing-wave features.

As described in section 2h, 2D snapshots of mode-1, M_2 SSHA are plotted for the northward component (Fig. 14a), the southward component (Fig. 14b), and their total (Fig. 14c). Regions where no clear north-south separation is possible are left white. As discussed in the work of Zhao and Alford (2009), the northeastward Hawaiian beam (Fig. 14a) originates from FFS and Nihoa Island (NI), two strong generation sites at the Hawaiian Ridge (Merrifield and Holloway 2002; Lee

et al. 2006). The low spatial resolution (250 km \times 250 km) of the altimetric estimates precludes the separation of the individual FFS and NI contributions. [Zhao and Alford (2009) show that the FFS and NI beams cross near 32°N.] Southward signals (Fig. 14b) can be tracked over 2000 km back to Amukta Pass (about 100 km in width, centered at 52.5°N, 188°E) in the Aleutian Islands. The combined signal (Fig. 14c) shows a phase discontinuity near 198°E, and a maximum aligned in the north-south direction to the west of that, between the dashed lines.

To examine the interference pattern, two plane waves are next constructed (Figs. 14d and 14e) by matching the observed amplitude, wavelength, phase, and propagation direction (values in Table 3) of the northbound and southbound signals. Their superposition (Fig. 14f) reproduces both the phase discontinuity and the “apparent beam” seen in the observed combined signals (Fig. 14c). This feature is similar to that to the south of the Hawaiian Ridge, which is caused by multiple sources at the ridge (Rainville et al. 2010). The parameters used are chosen

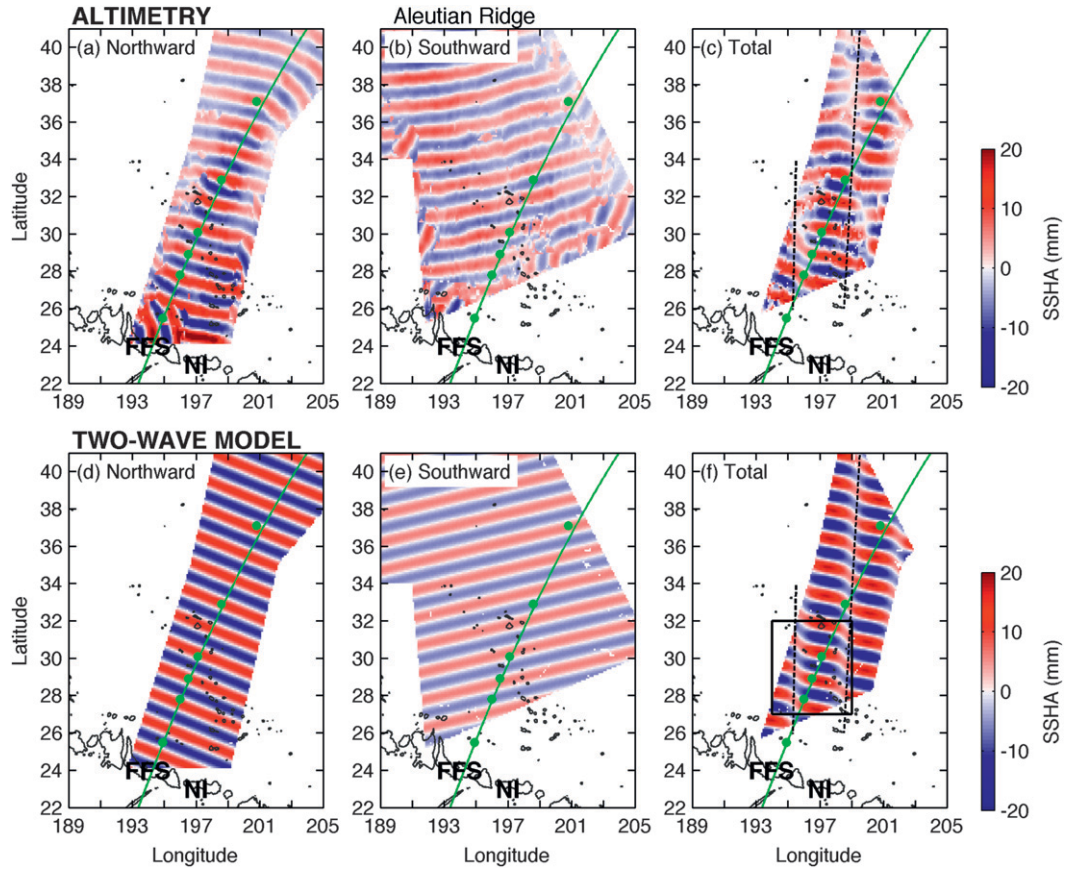


FIG. 14. Snapshots of SSHA from (top) altimetry and (bottom) the superposition of two plane waves. Altimetric M_2 SSHAs for (a) the northward constituents, (b) the southward constituents, and (c) their total. FFS and NI are labeled. Green dots and line indicate the IWAP moorings and T/P track 249, respectively. Snapshots of SSHA for a mode-1 wave traveling toward (d) the northeast, (e) the southeast, and (f) their sum. Amplitude, wavelength, direction, and phase values are given in Table 3. In (c),(f), dashed lines indicate an “apparent beam” resulting from their constructive interference.

to match the altimetric observations (Table 3). We will next examine the amplitude, phase, energy, and energy flux in a subregion (Fig. 14f, box) and compare these results with the moored observations.

The small-scale patterns in the amplitude, phase, energy, and energy flux of the interference pattern are next examined in the subregion 27° – 32° N, 194° – 199° E, and compared with the moored observations at MP2–MP4. For each wave, each of these quantities is simply related to SSHA (Chiswell 2006; Zhao and Alford 2009). The corresponding expressions for the superposed wave fields are more complicated owing to the cross terms in the velocity and pressure (Nash et al. 2004; Martini et al. 2007; Rainville et al. 2010). Here, a constant inertial frequency f at 28.9° N is taken, neglecting its small latitudinal change. The results for the amplitude, phase, energy, and flux are shown in Fig. 15: interference patterns are

presented in Figs. 15a–d, and comparisons with moored observations are given in Figs. 15e–h.

The amplitude and phase of the superposed signal shown in the snapshot in Fig. 14f are plotted in Figs. 15a and 15b. The amplitude displays a banded half-wavelength periodic structure, while the phase shows a twisted pattern. Plotted along the mooring array versus latitude, half-wavelength

TABLE 3. Parameters of plane waves that are used to simulate the Hawaiian and Aleutian beams.

Plane wave	Wavelength (km)	Amplitude (mm)	Direction ($^{\circ}$)	Phase* ($^{\circ}$)
Hawaiian beam	162	12	68	39
Aleutian beam	162	6	–77	297

* Initial phase at 32° N, 197° E with reference time 0000 UTC 1 Jan 1992.

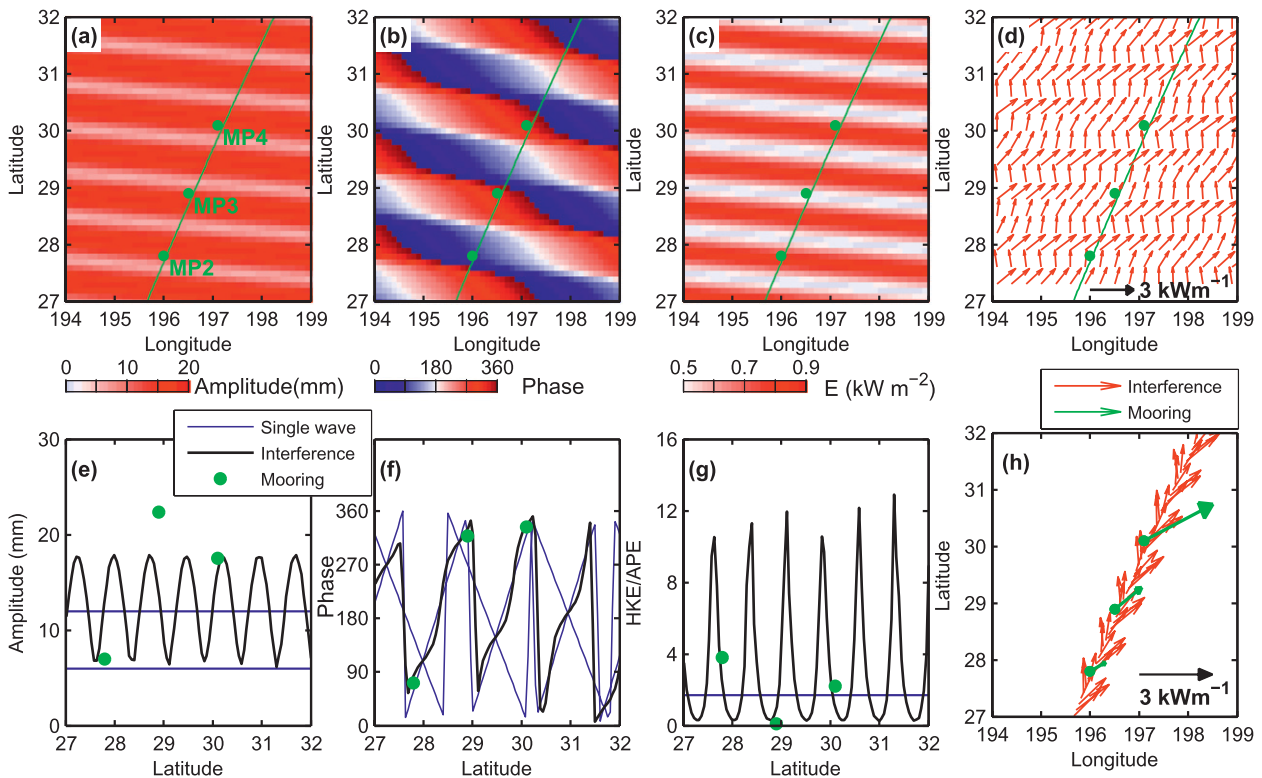


FIG. 15. Interference patterns from (a)–(d) two plane waves and (e)–(h) comparisons with moored observations along the track shown. (a) Amplitude. The green line and dots indicate T/P track 249 and the IWAP moorings, respectively. (b) Phase. (c) Energy. (d) Energy flux. (e) Amplitude of the individual plane waves (purple), their sum (black), and that from moored observations (green dots). (f) As in (e), but for phase. (g) As in (e), but for the HKE/APE ratio. The theoretical value for a semidiurnal wave is shown in purple. (h) As in (e), but for energy flux.

modulations are present in both quantities (Figs. 15e and 15f, black). Both are reminiscent of modulations observed in the along-track altimetric observations (Figs. 11a and 11b). For comparison, the individual northward and southward waves (purple) show constant amplitude and linearly increasing phase. The moored observations (green dots) agree very well with the two-wave simulated results, with the exception of the amplitude at MP3.

The simulated energy (Fig. 15c), HKE/APE ratio (Fig. 15g), and flux (Figs. 15d and 15h) all show banded interference patterns, demonstrating that their values are spatially variable rather than constant values for plane waves. HKE/APE ranges from 0.25 to 13 in this case (Fig. 15g, black), compared with a constant ratio (≈ 1.69 for M_2 at 28.9°) for free progressive plane waves (purple). Generally, the observed HKE/APE ratios at MP2–MP4 (Fig. 15g, green) agree with the two-wave simulation. Importantly, the superposed flux vector shows alternate bands of flux in the transverse direction that do not point away from either source (Nash et al. 2004; Alford and

Zhao 2007b; Martini et al. 2007). The observed veering and modulation of the moored flux vectors (Fig. 15h, green arrows) are generally consistent with the simulated fluxes (red arrows).

6. Summary

Observations of the semidiurnal internal tide from six highly resolved profiling moorings spanning 1400 km have been presented, with the aim of characterizing the internal tide's synoptic spatial structure and progression over a long distance. The collocation of the mooring array and one T/P track has enabled a direct comparison of the moored and altimetric SSHAs. We have thus obtained a qualitative picture of the semidiurnal internal tide from the mooring array that is well resolved in time and depth, and from the satellite altimeter that is well resolved in space along one track. The two complementary methods reveal complicated interference patterns caused by two internal tidal beams. Major findings include the following:

- In spite of a rich wave field of signals, the signature of the semidiurnal internal tide is clearly detectable in bandpassed moored measurements at all sites, up to 1600 km from the Hawaiian Ridge. Pronounced spring–neap cycles are visually apparent in the displacement and velocity at MP1 and in the energy and energy flux at all sites. Moving northeastward away from the ridge, internal tide signals generally become weaker (but not nonmonotonically) and less coherent with tidal forcing. The relative contribution from the higher-mode internal tide increases with range from the source. In spite of these events, the coherent mode-1 internal tide dominates and carries the majority (60%–88%) of the energy flux. Because the incoherent constituents are mostly random, the time-mean fluxes for the coherent and the bandpassed quantities are nearly the same.
- The coherent mode-1 internal tide signals are in excellent agreement with altimetric along-track signals up to MP5, with greater phase differences seen at MP6 being interpreted as different arrival times owing to mesoscale refraction during the mooring measurements. The tide’s propagation at group and phase speeds is examined using altimetric and moored measurements. The results agree well with theoretical values.
- The 2D interference pattern observed from the altimetry and moorings is consistent with the superposed radiation from Hawaii and the Aleutians. A simple two-wave model reproduces most of its observed features. Though the energy of the southward beam is only about 1/4 of the Hawaiian beam, it is sufficient to substantially modulate the signals, necessitating great care in their interpretation.

7. Discussion

A major motivation for the IWAP experiment was to determine the factors governing the attenuation of internal tides as they propagate away from their sources. A key long-term goal is determining the distribution of the dissipation of the internal tide. Toward this end, this study represents some progress, but also highlights the difficulty of the problem. Progress stems from the demonstration of the utility of combined moored–altimetric studies in diagnosing some of the aspects of the internal tide radiation field that would not be possible with either technique alone. The remarkable agreement between detection techniques as disparate as (a) an array of moorings deployed for less than 2 months, (b) a synoptic shipboard snapshot (Alford and Zhao 2007a), and (c) a harmonic fit from multiple years of remotely sense data offers hope that the spatial context offered by

the altimetry will be of great value in making future progress.

However, the complexity of the interference patterns, which are present even close to a known strong conversion region such as Hawaii, should give pause in simple interpretations. For example, in an ocean with a single point source, the internal tide’s attenuation can be measured as the range derivative of flux, accounting for cylindrical spreading. In the presence of multiple sources, the resulting interference pattern has a non-monotonic decay of flux even along “apparent beams” (Rainville et al. 2010). In certain regions, such as this one, where two sources dominate, sense can be made of the patterns. In other more complicated regions extreme care should be used in interpreting point measurements.

Additional complications arise because of the limitations of the altimetric technique (Zhao and Alford 2009). As discussed, the primary issues are the coarse spatial resolution, and the inability to resolve the temporally incoherent portion of the signals, which are expected to grow with increasing range from the source owing to mesoscale refraction by a time-variant mesoscale field. While this study makes it clear that direct comparisons can be made, a quantitative transfer function between the altimeter-observed internal tides and the in situ, time-variant internal tides is sorely needed. Only then can observed attenuation be associated with “true” dissipation and radial spreading. In the interim, the processes and degree of internal tide dissipation remain open questions, and altimetric signals remain a valuable tool for interpretation.

Acknowledgments. We thank the captain and crew of the R/V *Revelle* for their skill at sea. We also thank Eric Boget, Andrew Cookson, and Kim Martini for their hard work in designing, preparing, deploying, and recovering the moorings, and Tom Peacock and Paola Eccheverri for volunteering their time on the recovery cruise. Finally, we are grateful to Knut Aagard, Charlie Eriksen, Rebecca Woodgate, Craig Lee, and Elise Ralph for their generosity in lending mooring equipment. This work was supported by NSF Grant OCE-0424717.

APPENDIX

Errors

Errors arise from moorings’ imperfect vertical resolutions, the adequacy of which depends on the mooring geometry and the modal partitioning of the internal tide signals (Nash et al. 2005). Rainville and Pinkel (2006a) successfully determine mode-1 internal tide solutions from well-resolved measurements in the upper 800-m

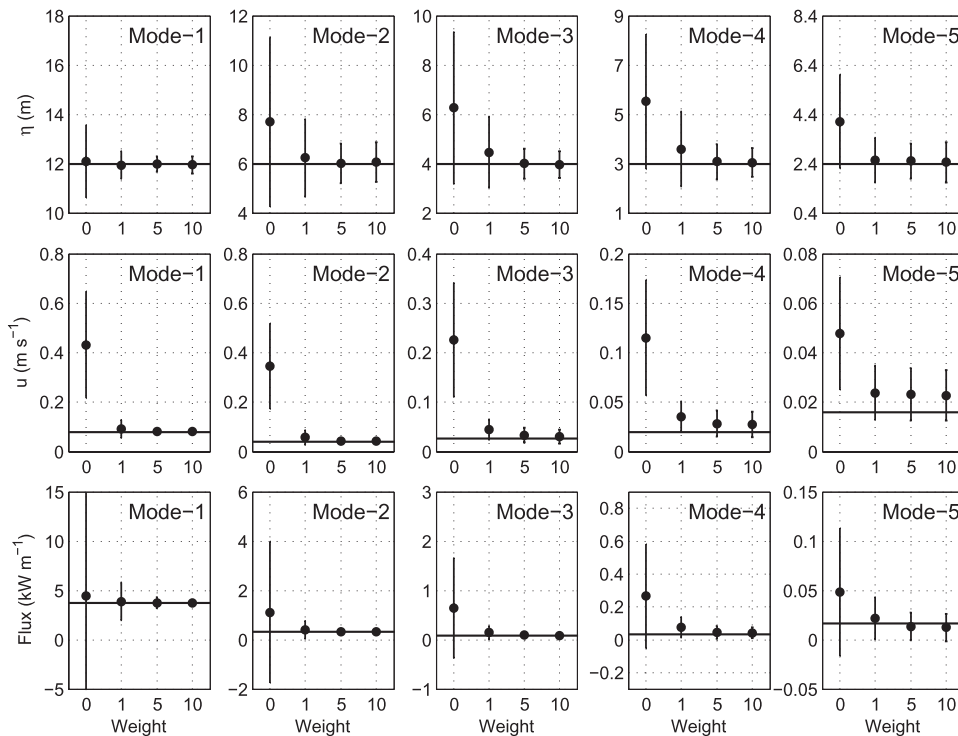


FIG. A1. Mean (circles) and standard error (bars) vs mode number (left to right) 1–5 and weighting of the 3000-m data for (top) displacement, (middle) velocity, and (bottom) flux, simulated using Monte Carlo methods following Nash et al. (2005). A synthetic internal tide is created by superposing 30 modes with a red spectrum in the vertical wavenumber (m) $\sim m^{-1}$. The horizontal lines represent the “true” values in the synthetic wave field.

water column alone. In IWAP, higher-mode signals render upper-column-only solutions extremely unreliable and even of the incorrect sign, as determined by comparison of the energy flux computed from full-depth

lowered ADCP–CTD time series (Fig. 1, blue dots) with the moored quantities (not shown). Following Nash et al. (2005), the magnitude of the effect is assessed with Monte Carlo simulations by running a synthetically

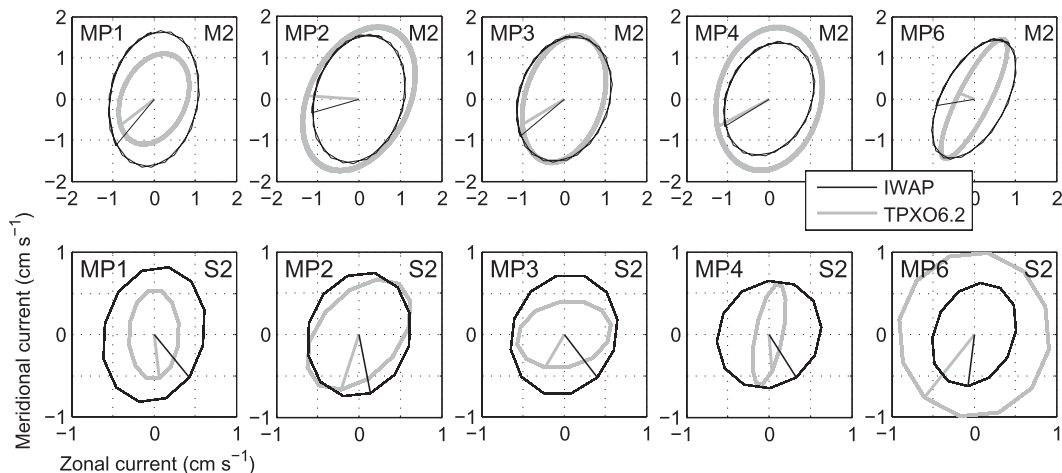


FIG. A2. Comparisons of barotropic tidal current ellipses from mooring measurements (black) and the TPXO6.2 tidal model (gray) for (top) M_2 and (bottom) S_2 ; (left to right) MP1 to MP6. The lines indicate current vectors at 0000 UTC 1 Jan 2006. MP5 is excluded due to its short profiling time. Note the scale difference between the top and bottom panels.

generated wave field past our mooring geometry (Fig. A1). As found by Rainville and Pinkel (2006a), mode-1 displacement is reliably estimated without deep data (see top-left panel of Fig. A1; weight = 0). However, our measurements at 3000 m are critical to constraining the fits for displacement modes ≥ 2 (top-right panels in Fig. A1), and all velocity modes (middle row of panels in Fig. A1). Here, a weight is added to the 3000-m data to increase their contributions in modal decomposition. Mode-1 fluxes (bottom row of panels Fig. A1) are hence unreliable (showing high bias and large error bars) when the deep data are excluded from calculation (weight = 0) but are otherwise insensitive to weighting. Corresponding fractional standard errors with a weight of 10 (taken in this paper) for each uncorrelated estimate are 8%, 30%, and 50% for the first three modes.

Building on the synthetic calculations, one means of assessing the reliability of the modal projection is to compare our estimates of barotropic tidal velocity [Eq. (6), mode = 0] with predictions from the TPXO6.2 tidal model (Egbert and Erofeeva 2002). The mooring-obtained M_2 and S_2 currents are ≈ 2 and ≈ 1 cm s^{-1} (Fig. A2, black). Agreement with TPXO6.2 (gray) is better for the M_2 constituent, presumably owing to the stronger signals. For M_2 , the amplitude, elliptical elongation, and phase are in good agreement with the model predictions. For S_2 , the moored amplitudes appear to be biased slightly high, and the phases fall slightly behind, at all locations (except for MP6 in amplitude). We interpret the general good agreement as evidence that the modal fits are partitioning energy reasonably into the appropriate modes.

REFERENCES

- Alford, M. H., 2003: Redistribution of energy available for ocean mixing by long-range propagation of internal waves. *Nature*, **423**, 159–162.
- , and Z. Zhao, 2007a: Global patterns of low-mode internal-wave propagation. Part I: Energy and energy flux. *J. Phys. Oceanogr.*, **37**, 1829–1848.
- , and —, 2007b: Global patterns of low-mode internal-wave propagation. Part II: Group velocity. *J. Phys. Oceanogr.*, **37**, 1849–1858.
- , J. A. MacKinnon, Z. Zhao, R. Pinkel, J. Klymak, and T. Peacock, 2007: Internal waves across the Pacific. *Geophys. Res. Lett.*, **34**, L24601, doi:10.1029/2007GL031566.
- Antonov, J. I., R. A. Locarnini, T. P. Boyer, A. V. Mishonov, and H. E. Garcia, 2006: *Salinity*. Vol. 2, *World Ocean Atlas 2005*, NOAA Atlas NESDIS 61, 182 pp.
- Berwin, R., 2003a: Along-track gridded sea surface height anomaly for TOPEX/Poseidon and Jason-1: User's reference manual. NASA/JPL Physical Oceanography DAAC, 9 pp.
- , 2003b: TOPEX/Poseidon sea surface height anomaly product: User's reference manual. NASA Physical Oceanography DAAC, 15 pp.
- Chiswell, S. M., 2002: Energy levels, phase, and amplitude modulation of the baroclinic tide off Hawaii. *J. Phys. Oceanogr.*, **32**, 2640–2651.
- , 2006: Altimeter and current meter observations of internal tides: Do they agree? *J. Phys. Oceanogr.*, **36**, 1860–1872.
- Cummins, P. F., J. Y. Cherniawsky, and M. G. G. Foreman, 2001: North Pacific internal tides from the Aleutian Ridge: Altimeter observations and modeling. *J. Mar. Res.*, **59**, 167–191.
- Doherty, K. W., D. E. Frye, S. P. Liberatore, and J. M. Toole, 1999: A moored profiling instrument. *J. Atmos. Oceanic Technol.*, **16**, 1816–1829.
- Dushaw, B. D., B. D. Cornuelle, P. F. Worcester, B. M. Howe, and D. S. Luther, 1995: Barotropic and baroclinic tides in the central North Pacific Ocean determined from long-range reciprocal acoustic transmissions. *J. Phys. Oceanogr.*, **25**, 631–647.
- Egbert, G. D., and R. D. Ray, 2000: Significant dissipation of tidal energy in the deep ocean inferred from satellite altimeter data. *Nature*, **405**, 775–778.
- , and —, 2001: Estimates of M_2 tidal energy dissipation from TOPEX/Poseidon altimeter data. *J. Geophys. Res.*, **106**, 22 475–22 502.
- , and S. Y. Erofeeva, 2002: Efficient inverse modeling of barotropic ocean tides. *J. Phys. Oceanogr.*, **32**, 183–204.
- Garrett, C., and E. Kunze, 2007: Internal tide generation in the deep ocean. *Annu. Rev. Fluid Mech.*, **39**, 57–87.
- Gill, A. E., 1982: *Atmosphere–Ocean Dynamics*. Academic Press, 662 pp.
- Hendry, R. M., 1977: Observations of the semidiurnal internal tide in the western North Atlantic Ocean. *Philos. Trans. Roy. Soc. London*, **286A**, 1–24.
- Klymak, J. M., and Coauthors, 2006: An estimate of tidal energy lost to turbulence at the Hawaiian Ridge. *J. Phys. Oceanogr.*, **36**, 1148–1164.
- Lee, C. M., E. Kunze, T. B. Sanford, J. D. Nash, M. A. Merrifield, and P. E. Holloway, 2006: Internal tides and turbulence along the 3000-m isobath of the Hawaiian Ridge. *J. Phys. Oceanogr.*, **36**, 1165–1183.
- Locarnini, R. A., A. V. Mishonov, J. I. Antonov, T. P. Boyer, and H. E. Garcia, 2006: *Temperature*. Vol. 1, *World Ocean Atlas 2005*, NOAA Atlas NESDIS 61, 182 pp.
- MacKinnon, J. A., and K. B. Winters, 2005: Subtropical catastrophe: Significant loss of low-mode tidal energy at 28.9°. *Geophys. Res. Lett.*, **32**, L15605, doi:10.1029/2005GL023376.
- Martini, K. I., M. H. Alford, J. D. Nash, E. Kunze, and M. A. Merrifield, 2007: Diagnosing a partly-standing internal wave in Mamala Bay, Oahu. *Geophys. Res. Lett.*, **34**, L17604, doi:10.1029/2007GL029749.
- Merrifield, M. A., and P. E. Holloway, 2002: Model estimates of M_2 internal tide energetics at the Hawaiian Ridge. *J. Geophys. Res.*, **107**, 3179, doi:10.1029/2001JC000996.
- Mitchum, G. T., and S. M. Chriswell, 2000: Coherence of internal tide modulations along the Hawaiian Ridge. *J. Geophys. Res.*, **105**, 28 653–28 661.
- Nash, J. D., E. Kunze, J. M. Toole, and R. W. Schmitt, 2004: Internal tide reflection and turbulent mixing on the continental slope. *J. Phys. Oceanogr.*, **34**, 1117–1134.
- , M. H. Alford, and E. Kunze, 2005: Estimating internal wave energy fluxes in the ocean. *J. Atmos. Oceanic Technol.*, **22**, 1551–1570.
- , E. Kunze, C. M. Lee, and T. B. Sanford, 2006: Structure of the baroclinic tide generated at Kaena Ridge, Hawaii. *J. Phys. Oceanogr.*, **36**, 1123–1135.

- Pawlowicz, R., B. Beardsley, and S. Lentz, 2002: Classical tidal harmonic analysis including error estimates in Matlab using T_Tide. *Comput. Geosci.*, **28**, 929–937.
- Rainville, L., and R. Pinkel, 2006a: Baroclinic energy flux at the Hawaiian Ridge: Observations from the R/P *FLIP*. *J. Phys. Oceanogr.*, **36**, 1104–1122.
- , and —, 2006b: Propagation of low-mode internal waves through the ocean. *J. Phys. Oceanogr.*, **36**, 1220–1236.
- , T. M. S. Johnston, G. S. Carter, M. A. Merrifield, R. Pinkel, P. F. Worcester, and B. D. Dushaw, 2010: Interference pattern and propagation of the M_2 internal tide south of the Hawaiian Ridge. *J. Phys. Oceanogr.*, **40**, 311–325.
- Ray, R. D., 1999: A global ocean tide model from TOPEX/Poseidon altimetry: GOT99.2, NASA Tech. Memo. 1999-209478, 58 pp.
- , and G. T. Mitchum, 1996: Surface manifestation of internal tides generated near Hawaii. *Geophys. Res. Lett.*, **23**, 2101–2104.
- , and D. E. Cartwright, 2001: Estimates of internal tide energy fluxes from Topex/Poseidon altimetry: Central North Pacific. *Geophys. Res. Lett.*, **28**, 1259–1262.
- Rudnick, D. L., and Coauthors, 2003: From tides to mixing along the Hawaiian Ridge. *Science*, **301**, 355–357.
- St. Laurent, L., and C. Garrett, 2002: The role of internal tides in mixing the deep ocean. *J. Phys. Oceanogr.*, **32**, 2882–2899.
- Wunsch, C., 1975: Internal tides in the ocean. *Rev. Geophys. Space Phys.*, **13**, 167–182.
- Zhao, Z., and M. H. Alford, 2009: New altimetric estimates of mode-1 M_2 internal tides in the central North Pacific Ocean. *J. Phys. Oceanogr.*, **39**, 1669–1684.